1 Title: The number of cytokinesis nodes in mitotic fission yeast scales with cell size

2 Wasim A. Sayyad[1] and Thomas D. Pollard[1,2, 3,*]

3 [1]Department of Molecular Cellular and Developmental Biology

4 [2]Department of Molecular Biophysics and Biochemistry

5 [3]Department of Cell Biology

6 Yale University, PO Box 208103

7 New Haven, CT 06520-8103 USA

8 *Correspondence: thomas.pollard@yale.edu

Abstract

Cytokinesis nodes are assemblies of stoichiometric ratios of proteins associated with the plasma membrane, which serve as precursors for the contractile ring during cytokinesis by fission yeast. The total number of nodes is uncertain, because of the limitations of the methods used previously. Here we used the ~140 nm resolution of Airyscan confocal microscopy to resolve a large population of small, unitary cytokinesis nodes in 3D reconstructions of whole fission yeast cells. Wild-type fission yeast cells make about 200 unitary cytokinesis nodes early in mitosis. Most, but not all of these nodes condense into a contractile ring. The number of cytokinesis nodes scales with cell size in four strains tested, although wide *rga4Δ* mutant cells form somewhat fewer cytokinesis nodes than expected from the overall trend. The surface density of Pom1 kinase on the plasma membrane around the equators of cells is similar with a wide range of node numbers, so Pom1 does not control cytokinesis node number. However, varying protein concentrations with the *nmt1* promoter showed that the numbers of nodes increase above a baseline of about 200 with the total cellular concentration of either kinase Pom1 or Cdr2.

Introduction

Cytokinesis nodes are stoichiometric assemblies of multiple proteins, which associate with the plasma membrane around the middle of fission yeast cells and polymerize actin filaments that form the cytokinetic contractile ring (Vavylonis et al., 2008). Similar assemblies containing myosin-II may form contractile rings in other cells (Beach et al., 2014; Henson et al., 2017; Hickson & O'Farrell, 2008; Werner et al., 2007). In fission yeast, cytokinesis nodes form from two distinct types of interphase nodes (Akamatsu et al., 2014). At the end of cytokinesis, type 1 nodes containing kinases Cdr1 and Cdr2 appear in a broad band around the middle of the daughter cells as SIN activity drops (Pu et al., 2015), and after cell division type 1 nodes remain stationary throughout the interphase of daughter cells (Akamatsu et al., 2014; Martin & Berthelot-Grosjean, 2009; Morrell et al., 2004; Moseley et al., 2009). Type 2 nodes containing the proteins Blt1p, Klp8p, Gef2p, and Nod1p (Jourdain et al., 2013; Martin & Berthelot-Grosjean, 2009; Morrell et al., 2004; Moseley et al., 2009; Ye et al., 2012) originate from the constricting contractile ring from the previous cell cycle and diffuse along the plasma membrane from the new ends of daughter cells. During the G_2 phase of the cell cycle, type 1 nodes capture diffusing type 2 nodes to form cytokinesis nodes (Akamatsu et al., 2014). During ten minutes prior to spindle pole body (SPB) separation, cytokinesis nodes mature by sequentially accumulating stoichiometric ratios of

40 myosin-II (Myo2 heavy chain and two light chains), IQGAP Rng2p and F-BAR Cdc15p
41 (Vavylonis et al. 2008, Wu et al 2006). At the time of SPB separation, smaller numbers of formin
42 Cdc12p join each node, where they nucleate and elongate actin filaments (Laporte et al., 2011; J.-
43 Q. Q. Wu et al., 2006). Interactions between actin filaments from one node and myosin-II in
44 adjacent nodes pull the nodes together into a contractile ring (Vavylonis et al. 2008). Interestingly,
45 10-12 min after SPB separation, high SIN activity disperses the Cdr2p-mEGFP from the
46 cytokinesis nodes into the cytoplasm (Akamatsu et al., 2014; Martin & Berthelot-Grosjean, 2009;
47 Morrell et al., 2004; Moseley et al., 2009).

48 In addition to being the assembly platforms for cytokinesis nodes, interphase nodes are
49 critical for timing cell division. During interphase cells grow linearly at their tips (Fantes & Nurse,
50 1977; Moreno et al., 1989) until they reach a threshold size at twice the initial cell length (Gu &
51 Oliferenko, 2019; Neumann & Nurse, 2007). During this period, the interphase node components
52 also double in number (Allard et al., 2018; Pan et al., 2014). Interphase nodes are thought to sense
53 the cell surface area to control cell size at the time of division (Facchetti, Knapp, Chang, et al.,
54 2019; Pan et al., 2014).

55 In spite of their central role in the cell cycle, quantitative analysis of nodes has been
56 challenging, largely due to their heterogeneity observed by fluorescence microscopy. Rather than
57 appearing as a uniform population of spots, the fluorescence from node markers ranges from tiny
58 dim spots to much larger and brighter particles both during interphase (Moseley et al., 2009) and
59 mitosis (Vavylonis et al., 2008). Histograms of fluorescence intensity per node show that small,
60 dim nodes predominate, although the eye of the observer is drawn to larger, more intense spots
61 (Akamatsu et al., 2017). Many studies ignored dim nodes entirely.

62 Single-molecule localization super-resolution microscopy (SMLM) by Laplante et al.
63 (Laplante et al., 2016) explained the heterogeneity of node intensities and sizes. The 35 nm
64 resolution of this method revealed that cytokinesis nodes in live cells are much smaller (<100 nm)
65 than their diffraction-limited images in confocal micrographs. These particles are uniform in size
66 and contain stoichiometric ratios of proteins, each with a distinct localization. Some of these tiny,
67 single nodes are so close together that they have twice or three times the numbers of localizations
68 of unitary nodes, accounting for the variation in node intensity in confocal micrographs. Blurring
69 the super-resolution images of nodes with the point spread function of a confocal microscope

reproduced the heterogeneous mixtures of sizes and intensities. SMLM showed that the two types of interphase nodes are also tiny structures that tend to form clusters with twice or three times the number of localizations of single nodes (Akamatsu et al., 2017). Dim nodes predominate in confocal micrographs of interphase cells. In favorable cases (such as the abundant protein Cdr2) histograms of node intensities have higher intensity peaks corresponding to multiples of these dim spots, which Akamatsu et al. called ”unitary nodes” corresponding to Laplante’s single nodes.

This lack of resolution of individual nodes has compromised efforts to count cytokinesis nodes. Vavylonis et al. (Vavylonis et al., 2008) counted 63 ±10 cytokinesis nodes tagged with Rlc1p-3GFP in the broad bands of wild-type cells in 3D reconstructions of z-series acquired by spinning disk confocal microscopy. Nodes with low intensities grouped in one main peak; a higher intensity peak was attributed to pairs and clusters of unresolved nodes. Deng & Moseley (Deng & Moseley, 2013) applied deconvolution to images obtained in wide-field microscopy and counted ~52–106 interphase nodes tagged with Cdr2-mCherry. Pan et al. (Pan et al., 2014) used the Find Maxima macro function in ImageJ to find pixels with maximum intensity in maximum projection images and counted <50 interphase nodes and noted that the number scaled with cell length. However, they ignored dim nodes by choosing the only pixels in ROI with intensities greater than approximately twice the mean background intensity. Using the same scaled fire LUT plugin in ImageJ Willet et al. (Willet et al., 2019) measured ≤ 15 nodes marked with Mid1 in wild-type cells that had a yellow, orange, or white intensity but did not count dim purple or red intensity nodes. Allard et al. (Allard et al., 2018) used the superior (140 nm) resolution of Airyscan microscopy and an automated particle tracking plugin to count ~50 nodes tagged with Cdr2-mEGFP during interphase. However, the algorithm used in the plugin was designed to find only local intensity maxima and did not count the dim nodes with low intensities.

In principle, one should be able to identify and count every unitary node in a cell by SMLM, but the underlying strategy to collect the data has precluded this direct approach in living cells with fluorescent proteins. Only a thin slice of the cell is imaged before all of the proteins are irreversibly photobleached. Therefore, Laplante et al. (Laplante et al., 2016) used this limited sample to estimate the number of cytokinesis nodes in fission yeast broad bands. One approach was to measure the local density of nodes in a 400 nm optical section from the top or bottom of the cell and then to extrapolate this density around the equator, giving ~140 total nodes for five

100 different tagged proteins (Mid1, Rlc1, Cdc15, Myo2, and Rng2). The second method was to blur
101 the SMLM images with the point spread function to simulate a confocal image. This resulted in
102 about half the unitary nodes being blurred together, so the 65 nodes counted by Vavylonis et al.
103 (Vavylonis et al., 2008) represented roughly 130 unitary nodes.

104 Accurate measurements of node numbers are important for two reasons. First, the number
105 is a key parameter in computer simulations to test ideas about the mechanisms of contractile ring
106 assembly and constriction. Second, estimates of the number of molecules per node have relied on
107 measuring the total numbers of each protein in the broad band of nodes and then dividing by the
108 number of nodes (Laplante et al., 2016; Vavylonis et al., 2008).

109 We aimed to make a definitive count of the number of cytokinesis nodes and determine
110 how this number varies with cell size. Our strategy depended on three considerations. First, we
111 used the scaffold protein Blt1 tagged with mEGFP to mark cytokinesis nodes, since it is the only
112 protein associated with nodes throughout the cell cycle. Other node proteins join or leave nodes
113 throughout mitosis. For example, Myo2, Rng2, and Cdc12 arrive during 10 min prior to the
114 separation of spindle pole bodies, and Mid1 and Cdr2 depart as contractile rings form and mature.
115 Second, we collected data during a short time interval of 2-5 min after the spindle pole bodies
116 divided, when the nodes are still in the form of a broad band, to avoid the compositional changes
117 that occur continuously during the cell cycle. All of the nodes considered here were within minutes
118 of condensing into contractile rings. Third, following Allard et al. (Allard et al., 2018) we used
119 Airyscan microscopy to image cytokinesis nodes. The higher resolution of Airyscan allowed us to
120 detect more dim cytokinesis nodes than resolved by conventional confocal microscopy. We
121 calculated the total number of cytokinesis nodes from the ratio of the total intensity of Blt1-mEGFP
122 around the equator to the average intensity of unitary nodes.

123 We report that wild-type fission yeast cells have about 200 cytokinesis nodes in a broad
124 band at the equator. About three-fourths of these cytokinesis nodes condense into the contractile
125 ring. The number of cytokinesis nodes during early mitosis scales directly with cell size in strains
126 that are smaller or larger than wild-type cells. The kinases Pom1 and Cdr2 modulate the number
127 of nodes set by the cell size.

128 **Results**

129 **Blt1 as a cytokinesis node marker**

130 Two challenges complicate counting cytokinesis nodes in fission yeast. First, they form over 10
131 minutes and then condense into a contractile ring within 10-12 min after the spindle pole body
132 divides. Second, the protein composition of cytokinesis nodes changes dramatically during this 22
133 minute period (Bhatia et al., 2014; Lee & Wu, 2012; Pan et al., 2014; Rincon et al., 2014). The
134 numbers per node of cytokinesis node proteins formin Cdc12, F-BAR Cdc15, anillin Mid1,
135 myosin-II Myo2, and IQGAP Rng2 change rapidly as cytokinesis nodes form from interphase
136 nodes (10 min prior to spindle pole body separation), condense into contractile rings (10-12 min
137 after spindle pole bodies separate) and then mature (over the next 15 min) (J.-Q. Wu & Pollard,
138 2005).

139 We solved the first issue by studying live cells with spindle pole bodies marked with Sad1-
140 RFP. We selected cells with two narrowly separated spindle pole bodies and well-dispersed nodes
141 in a broad band around the equator.

142 We dealt with the second issue by marking nodes with the scaffold protein Blt1 tagged
143 with mEGFP. Blt1 is the only protein known to persist in nodes throughout the cell cycle, so it is
144 found in interphase nodes, cytokinesis nodes, and contractile rings (Akamatsu et al., 2014; Goss
145 et al., 2014; Moseley et al., 2009). Therefore, Blt1 is the only reasonable marker to measure the
146 number of cytokinesis nodes. The fluorescent proteins were integrated into the haploid genome to
147 ensure that all copies of each protein were tagged and expressed at normal levels.

148 **Airyscan fluorescence microscopy resolves dim unitary cytokinesis nodes in a broad band**

149 We used a Zeiss Airyscan fluorescence microscope to acquire 40 Z-slices covering the entire
150 volume of cells to measure the total and local fluorescence of Blt1-mEGFP in wild-type fission
151 yeast cells in 2-3 s. The frame size and pixel dwell time were adjusted so that motions of
152 cytokinesis nodes (20 nm/s; (Vavylonis et al., 2008)) did not blur the images during image
153 acquisition. Cytokinesis nodes appeared as a broad band of fluorescence spots in the cortex around
154 the middle of mitotic cells with two SPBs. The fluorescence intensities of these spots ranged from
155 very bright to dim (Figure 1 A, upper panel).

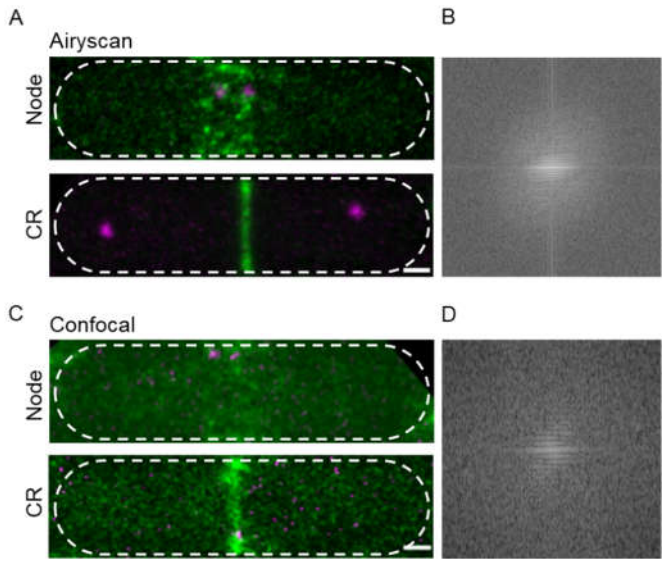

Figure 1. Comparison of Airyscan and confocal images of cytokinesis nodes and contractile rings in wild-type fission yeast cells expressing Blt1-mEGFP (green) and Sad1-RFP showing two spindle pole bodies (magenta). (A) Airyscan images. Max projections of 40 Z- slices. The upper cell has a broad band of cytokinesis nodes (green). The lower cell has a contractile ring. (B) Fast Fourier transform of the image in lower panel A, green channel. (C) Confocal images. Max projections of 20 Z-slices of confocal fluorescence with 0.6 AU+8X averaging + iteratively constrained deconvolution micrographs. The upper cell has broad band of cytokinesis nodes. The lower cell has a contractile ring. (D) Fast Fourier transform of the image in lower panel C, green channel). The scale bar is 1 µm.

To compare the high resolution and sensitivity of Airyscan to a conventional laser scanning confocal microscope, we used the same Airyscan detector in confocal mode with a pinhole of 0.6 AU, 8X line averaging + linear constrained iterative deconvolution, and 2X laser intensity to compensate for the lower signal to noise ratio as assessed previously (Kolossov et al., 2018). Large nodes stood out in the confocal images, but the higher background noise made it difficult to detect the dim cytokinesis nodes in broad bands. Contractile rings were brighter and narrower in Airyscan than confocal images (Figure 1 A and C, lower panels). Fast Fourier transform analysis of images of cells with contractile rings showed that Airyscan retrieved higher frequencies and more extensively distributed information. The horizontal line in the frequency domain of the Airyscan image corresponds to the contractile ring (Figure 1B), which was absent in the frequency domain of the confocal image (Figure 1D). This shows that with 3D reconstruction ability similar to confocal microscopy, Airyscan imaging can resolve small, dim unitary cytokinesis nodes. We interpret the small nodes satisfying two ROI conditions (Please see methods Section) as unitary nodes, while the brighter nodes consist of two or more unitary nodes (Akamatsu et al., 2017; Laplante et al., 2016) located too closely to be resolved.

179 Time-lapse imaging showed that cytokinesis nodes of all sizes, including unitary nodes,
180 condensed into bigger and brighter nodes as they coalesce into a contractile ring during 10-12 min
181 after separation of the SPBs as described for the brighter fraction of the population of nodes by
182 confocal microscopy (Vavylonis et al., 2008). Neither the Airyscan nor confocal microscopy
183 resolved cytokinesis nodes known to be present in contractile rings (Figure 1A and C, lower
184 panels) by single-molecule localization microscopy (Laplante et al., 2016).

185 **Counting cytokinesis nodes in the broad band**

186 The methods section explains how we used the three-dimensional distribution of fluorescence of
187 spots around the equator to identify nodes (Figure 2A) and measure their fluorescence. To qualify
188 as a node, the fluorescence had to be confined in the X-Y plane within a circle 12-pixels (0.5 µm)
189 in diameter and in the Z direction to 7 z-slices of 170 nm (1.1 µm). The total fluorescence within
190 the 12-pixel diameter circle in 7 z-slice images was sum projected and measured as a node
191 fluorescence (Figure 2B). From the same sum projected image we calculated the average
192 fluorescence from 8 equivalent volumes of cytoplasm near each cell tip where nodes were absent
193 (Figure 2B). The fluorescence of each candidate node was its total fluorescence minus the average
194 cytoplasm fluorescence.

195 We measured the fluorescence of 364 nodes in 24 mitotic, wild-type cells satisfying the
196 aforementioned ROI conditions and plotted a histogram to determine the distribution of intensities
197 and the average fluorescence intensity (Figure 2D). Gaussian fitting and D'Agostino-Pearson's
198 normality test showed that fluorescence intensities of these cytokinesis nodes formed a broad,
199 normal distribution ($p = 0.1$) with a slightly longer high-intensity tail. We considered the 92%
200 nodes with the fluorescence under the gaussian peak as unitary nodes, while the 8% of nodes with
201 fluorescence greater than twice the peak of the gaussian curve (~4800 AU) are likely unresolved
202 binary nodes. To calculate the mean value of fluorescence of unitary nodes we considered only the
203 node with fluorescence values less than or equal to twice the peak of the gaussian curve fitted to
204 the distribution and obtained the mean value of 2409 and a standard deviation (SD) of 961.

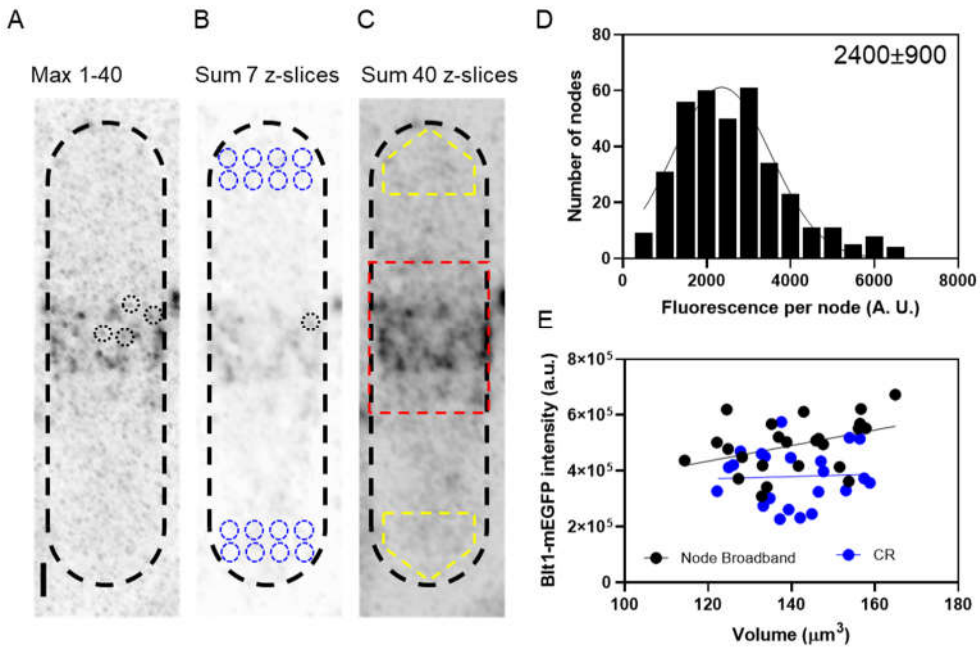

Figure 2. Counting cytokinesis nodes in broad bands and contractile rings of wild-type cells expressing Blt1-mEGFP. (A) Reverse contrast fluorescence micrograph of Figure 1A upper panel. Black dotted circles are nodes selected for fluorescence measurements. (B) Reverse contrast fluorescence micrograph of a sum projection of seven slices of the cell in panel A. Black dotted circles mark spots selected to measure the fluorescence of unitary nodes and blue dotted circles mark cytoplasmic regions selected to measure background fluorescence. (C) Reverse contrast fluorescence micrograph of a sum projection of 40 Z-slices of the cell in panel A. The red rectangle outlines the region used to measure the total node broad band intensity and the yellow polygonal area marks the area chosen to measure background intensity to subtract from the broad band area. (D) Histogram of the distribution of fluorescence intensities of a sample of 364 cytokinesis nodes from 24 cells. The continuous curve is a fit of a Gaussian distribution to the data ($R^2 = 0.9$) with the mean value of 2400 and SD of 900. (E) The total Blt1-mEGFP intensity in broad bands (Black points, 24 cells) and contractile rings (Blue points, 22 cells) as a function of cell volume. The slopes of the corresponding linear regressions are not significantly different from zero ($p = 0.06$, for node broadband, and $p = 0.8$ for contractile rings).

We estimated on average 200 unitary nodes in the broad bands of wild-type fission yeast cells from the ratio of total intensity (corrected for cytoplasmic background) of Blt1-mEGFP in a broad band around the equator of a given cell to the intensity of Blt1-mEGFP in an average unitary node, 2400 ±900 AU (Figure 2D). We used 3D reconstructions of stacks of Airyscan images to measure the total fluorescence of all the cytokinesis nodes around the equator of each cell for direct comparison with the average fluorescence of unitary nodes.

D'Agostino-Pearson's normality test showed that the values of these ratios of total broad band fluorescence to the fluorescence of a unitary node were distributed normally ($p = 0.8$) with a mean of 200 and SD of 40 nodes per cell (Figure 2E). This number is more than three-fold that

228 reported by Vavylonis et al. (Vavylonis et al., 2008) from spinning disk confocal images where
229 only bright cytokinesis nodes were resolved.

230 **Mutant strains with a range of sizes**

231 Wild-type fission yeast cells undergo mitosis when they reach lengths of 12-15 μm, but their actual
232 volumes vary from about 110 μm^3 to 170 μm^3. Within this naturally occurring variation in sizes,
233 the number of unitary nodes in the broad band tended to increase with cell volume (Figure 2E).
234 This observation motivated us to count the numbers of cytokinesis nodes in mitotic cells with a
235 range of sizes. We used five different mutant strains, described in the following paragraphs, and
236 hydroxyurea, to create cells that varied in volume from 24 μm^3 to 450 μm^3 during mitosis (Figure
237 3).

238 The Wee1 kinase catalyzes the phosphorylation of Cdc2/Cdk1 to prevent cells from
239 entering mitosis (Russell & Nurse, 1987). At the restrictive temperature of 36°C, *wee1-50* cells
240 enter mitosis prematurely, so they are smaller than normal (Paul Nurse, 1975). After 4 h at the
241 restrictive temperature, the average cell length of *wee1-50* mutant cells (7.8 ±1 μm) was about half
242 the average length of wild-type cells (14 ± 1 μm) (Figure 3C). The diameter of *wee1-50* mutant
243 cells (3.7 ±0.2 μm) was the same as wild-type cells (3.7 ±0.1 μm). When released to the permissive
244 temperature, most cells started to form a contractile ring in 10-15 min. The broad band of nodes
245 looked more dispersed in these cells than in other strains.

246 The Cdc25 phosphatase removes the inhibitory phosphates added by Wee1 from
247 Cdc2/Cdk1 to allow cells to enter mitosis (P Nurse, 1990; Russell & Nurse, 1986, 1987). At the
248 restrictive temperature of 36°C, *cdc25-22* mutant cells arrest at the G_2/M transition but continue
249 growing at both ends. We varied the time at 36°C to obtain a range of lengths. After 4-6 h at 36°C
250 cells were 26.9 ±5.8 μm long, twice the average length of wild-type cells but did not differ
251 significantly in diameter (3.9 ±0.1 μm) (Figure 3A) and had broader equatorial bands with more
252 cytokinesis nodes (Vavylonis et al., 2008). The *cdc25-22* mutant cells produced a wide range of
253 cell sizes, so we grouped them by size. When released to the permissive temperature, most of the
254 cells synchronously entered mitosis within 1 h and formed a broad band of cytokinesis nodes.

255 The RhoGAP Rga4 localizes to the division site of cells and inactivates the GTPase Cdc42
256 (Das et al., 2007). Cells with deletion mutations of *rga4* are shorter (11.6 ± 1.0 μm) but have larger

diameters (4.4 ±0.2 µm) than wild-type cells (Das et al., 2007; Tatebe et al., 2008) (Figure 3D). Treating *rga4Δ* cells with 15 mM hydroxyurea for 4-6 h inhibited DNA synthesis by inactivating ribonucleoside reductase (Krakoff et al., 1968) and arrested the cells in the S phase during which they grew longer (J.M.MitchisonJ.Creanor, 1971) (Figure 3F). On the other hand, RhoGAP Rga2 localizes to growing cell tips and inactivates the Rho2 GTPase (Villar-Tajadura et al., 2008). Deletion of *rga2* does not change the cell length but decreases the cell diameter (3.4 ±0.2 µm) (Villar-Tajadura et al., 2008) (Figure 3E).

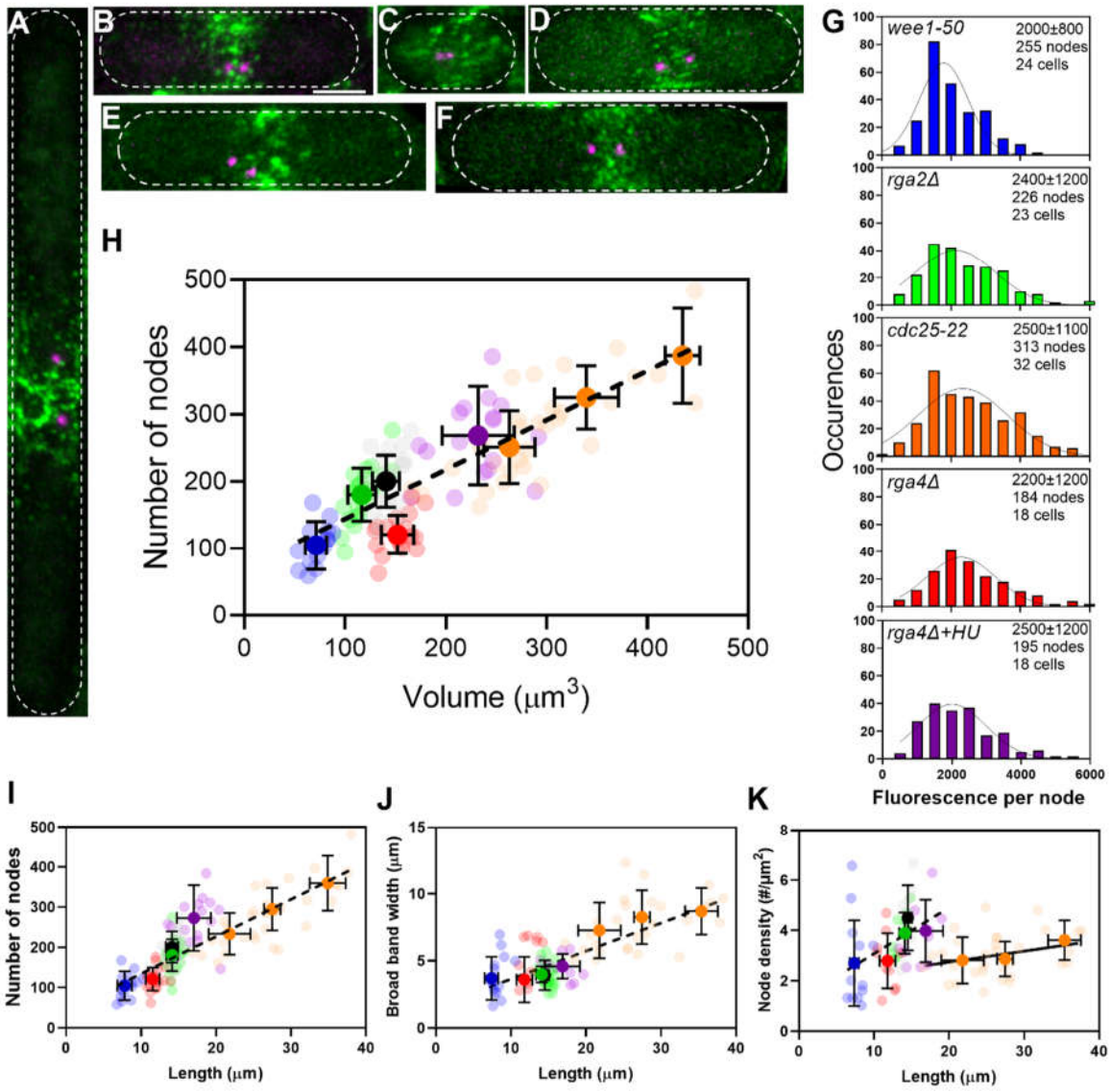

Figure 3. The number of cytokinesis nodes scales with the size of the cell. (A-F). Maximum intensity projections of Airyscan images 40 Z-sections of fission yeast cells expressing Blt1-mEGFP and Sad1-RFP showing two spindle pole

bodies (magenta). The scale bar is 3 µm. (A) *cdc25-22*; (B) wild type; (C) *wee1-50*; (D) r*ga4Δ*; (E) *rga2Δ*; and (F) *rga4Δ*+HU at 25°C. (G) Histograms of the distributions of fluorescence intensities of small nodes in five different strains. Wild type is also shown in Fig. 2C. Insets show average unitary node fluorescence intensity ± SD for each strain. Tukey's multiple comparison test showed that *wee1-50* differs significantly from the other strains with p <0.005. (H-K) Relationships between parameters (numbers, broad band width and densities) and cell size parameters in five strains: (●) *wee1-50* (n = 16 cells); (●) *rga2Δ* at (n = 23 cells); (●) wild type at (n = 24 cells); (●) r*ga4Δ* at (n = 17 cells); and (●) *rga4Δ*+HU (n = 17 cells) at 25°C. All measurements for each strain are collected in one bin except for (●) *cdc25-22* cells, which are divided into three volume bins: 200-300 µm^3, n = 18 cells; 300-400 µm^3, n = 13 cells; >400 µm^3, n = 4 cells and three length bins: 15-25 µm, n = 14 cells; 25-30 µm, n = 10 cells; 30-40 µm, n = 7 cells. The transparent symbols are measurements of individual cells. The solid symbols are the mean numbers of node parameters. Except for the *cdc25-22* cells, the vertical error bars show the SD of the mean numbers and horizontal error bars the SD of the lengths. For the *cdc25-22* (volume > 400 µm^3) cells the error bar is the range. The dashed black lines are linear regressions using all the data points. (H) Node number vs. cell volume. The slope of the linear regression (black dashed line) is significantly nonzero (P <0.0001; R^2 =0.6). (I) Node number vs. cell length. The slope of the linear regression (black dashed line) is significantly nonzero (P <0.0001; R^2 = 0.6). (J) Width of node broad band as a function of cell length. The slope of the linear regression (black dashed line) is significantly nonzero (P <0.0001; R^2 = 0.5) (K) Node density on the cortex of the broadband area as a function of cell length. The slope of the linear regression (black dashed line) is significantly nonzero (P = 0.001; R^2 = 0.18). The slope of the linear regression (black line) is significantly zero (P = 0.1; R^2 = 0.08).

Numbers of unitary cytokinesis nodes in a broad band scale with cell size

After correcting for cytoplasmic background fluorescence, we measured the total Blt1 fluorescence in the broad band around the equator of each cell (Figure 2). Assuming that this Blt1 is part of unitary nodes, we estimated the numbers of unitary cytokinesis nodes in the broad bands by dividing the total Blt1 fluorescence around the equator by the average intensity of the unitary nodes in that strain. The distributions of intensities Blt1 fluorescence of cytokinesis nodes were similar (around 2500 AU) in wild-type cells (Figure. 2C) and three of the experimental strains (Figure. 3G). The *wee1-50* mutant cells were an exception with an average node intensity of 2000 ±800, 80% of the others (Figure 3G). The cytokinesis nodes around the middle of the cells were more dispersed in the *wee1-50* mutant strain, so the broad band was less distinct than in other strains (Figure. 3A-F).

The numbers of cytokinesis nodes in the broad band of our sample of 129 cells were strongly correlated with cell volume (Figure 3H) with a slope of about 1 node per µm^3 of volume. This line does not extrapolate to the origin. Plots of the same data on node numbers vs. cell length (Figure. 3I) or surface area (Figure 3—figure supplement 1, A) showed the same linear relationship seen for cell volume, but the node numbers did not correlate with cell diameter (Figure 3—figure supplement 1, B)

304 Comparing the numbers of cytokinesis nodes in the broad band of wild-type cells, *rga4Δ*
305 cells, and *rga2Δ* cells provided data on the effect of cell diameter on the number of cytokinesis
306 nodes. The number of cytokinesis nodes in long, narrow *rga2Δ* cells (180 ±40) was
307 indistinguishable from wild-type cells (200 ±40) and aligned with the data from the other strains
308 in plots of node number vs. length and volume. On the other hand, the short, wide *rga4Δ* cells had
309 fewer cytokinesis nodes (116 ±30) than the wild-type and *rga2Δ* mutant cells with similar volumes
310 (Figure 3H). The *rga4Δ* cells grew longer in 15 mM hydroxyurea for 4-6 h and had the same
311 number of nodes per volume as the other strains (Figure 3H).

312 The cells might use two strategies to accommodate a total number of nodes in broad band
313 determined by their size. Either the surface area (width) of the broad band or the density of nodes
314 might increase with the total node number. We observed both. The very large *cdc25-22* mutant
315 cells simply expanded the width of the broad band in proportion to the number of nodes, while the
316 density of nodes increased with their numbers in the other strains of freely cycling cells (Figure
317 3J-K).

318 We measured the total Blt1-mEGFP fluorescence of the contractile rings of each strain
319 after cytoplasmic background subtraction to check if it also increase with cell size. The total Blt1-
320 mEGFP fluorescence in contractile rings increased with cell volume but was about 25% lower than
321 the total Blt1-mEGFP in the cytokinesis nodes in broad bands of wild-type cells and 25-50% less
322 in the contractile rings of *cdc25-22, wee1-50, and rga2Δ* mutant cells than in their broad bands.
323 On the other hand, *rga4Δ* mutant cells incorporated most of the Blt1-mEGFP in cytokinesis nodes
324 in the broad band into their contractile rings (Figure 3–figure supplement 2, A). Surprisingly,
325 the total Blt1-mEGFP fluorescence in the contractile rings of *cdc25-22* mutant cells did not
326 increase with cell volume, so the largest of these cells had as little as ~50 % of the cytokinesis
327 node Blt1-mEGFP fluorescence in their contractile rings. In contrast, like wild-type cells, *cdc25-*
328 *22* mutant cells did recruit mEGFP-Myo2 in their contractile rings in proportion to their volumes
329 (Figure 3–figure supplement 2, B).

330 **Does Pom1 control the number of cytokinesis nodes?**

331 We performed two types of experiments to investigate the relationship between the membrane-
332 bound Pom1 kinase and the number of cytokinesis nodes. Concentrating Pom1 at the poles depends

333 on microtubules that transport the polarity proteins Tea1 and Wsh3/Tea4 to the poles (Bähler &
334 Pringle, 1998; Martin & Berthelot-Grosjean, 2009; Moseley et al., 2009; Tatebe et al., 2005). First,
335 we measured the distributions of Pom1 in cells with a wide range of sizes by time-lapse, spinning
336 disk confocal microscopy (Figure. 4). The five strains were wild-type, *rga4Δ*, *rga2Δ*, *cdc25-22,*
337 and *wee1-50*. The cells expressed Pom1-GFP along with Sad1-RFP to identify mitotic cells with
338 two SPBs and Blt1-mCherry to track nodes. Second, we varied the concentration of Pom1 and
339 measured the number of nodes (Figure 5).

340 Figure 4A shows time series of fluorescence micrographs of individual cells from three
341 strains paired with scans of the fluorescent intensity of Pom1-GFP along the lengths of these cells,
342 while Figure 4B shows the average distributions of Blt1-mCherry plus Sad1-RFP (magenta) and
343 Pom1-GFP (green) along the lengths of 7-9 mitotic cells of the five different strains. To our
344 knowledge, this is the first time that the distribution of Pom1 was documented in cells with such a
345 wide range of sizes (lengths of 8 to 40 μm).

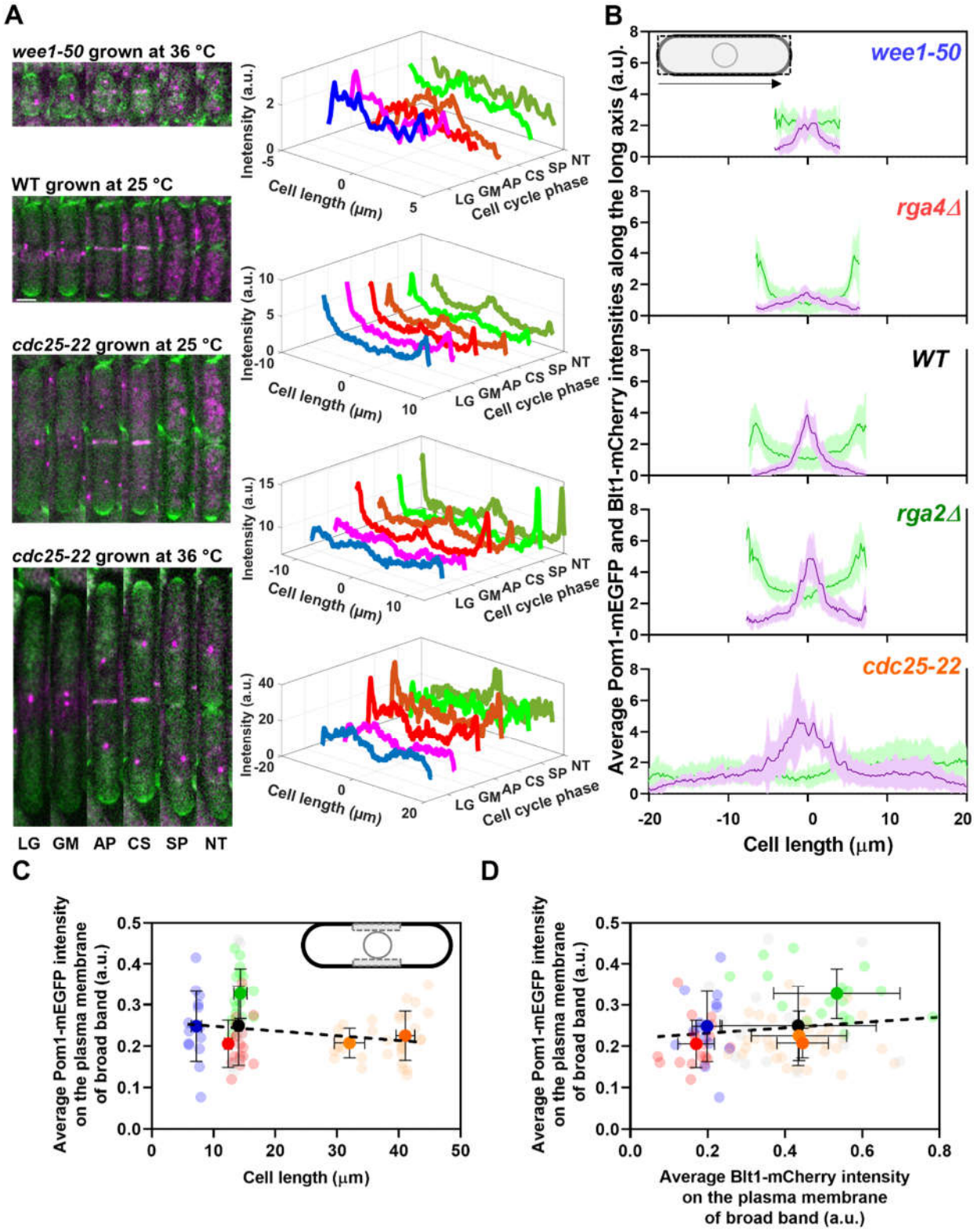

Figure 4. Distributions of Pom1 and Blt1 in cells that differ in size. (A) Distribution of Pom1 in wild type, *wee1-50,* and *cdc25-22* mutant cells. Each strain expressed Pom1-GFP and Blt1-mCherry-Sad1-RFP from their native loci. Each panel has two parts: (left) sum projected confocal images of 15 Z slices of wild-type cells taken at different

phases of life cycle abbreviated as LG (late G_2), GM (G_2/M), AP (anaphase), CS (constriction), SP (separation) and NT (new end take off); and (right) time series of plots of the average intensity of Pom1-GFP fluorescence along the length of the cells. Scale bar 3 µm. (Top panel) *wee1-50* grown at 36ºC and imaged at 22ºC. (Second panel) Wild-type cells were grown at 25ºC and imaged at 22ºC. (Third panel) *cdc25-22* mutant cells grown at 25ºC and imaged at 22ºC. (Bottom panel) *cdc25-22* mutant cells grown at 36ºC for 4 h before imaging at 22ºC. (B) Distributions of Pom1 and Blt1 in cells at the G_2/M transition measured by confocal microscopy of wild-type and four mutant strains. Cells were grown at 25°C and imaged at 22°C: (●, n = 9 cells) WT, (●, n = 7 cells) *wee1-50*, (●, n = 8 cells) *cdc25-22*, (●, n = 9 cells) *rga2Δ* and (●, n = 9 cells) *rga4Δ* mutant cells. Continuous lines are average fluorescence intensities of Blt1-mCherry-Sad1-RFP (magenta) and Pom1-GFP (green) across the full width of the cells and along the lengths of the cells. Light vertical bars are SD's. (C) Average Pom1-mEGFP intensity per pixel along the plasma membrane across the broad band of nodes in the middle focal plane of the cells as a function of the lengths of the cells. The inset shows the rectangle three pixels wide and the length of the broad band of nodes used to make the measurements. The slope of the linear regression (black dotted line) is significantly zero ($P = 0.07$; $R^2 = 0.03$). (D) Graph of the average Pom1 -mEGFP intensity per pixel vs the average Blt1-mCherry intensity per pixel along the plasma membrane in the middle focal plane of the cells (as in the inset of panel C). The slope of the linear regression (black dotted line) is significantly zero ($P = 0.13$; $R^2 = 0.02$).

Wild-type cells imaged at 22°C concentrated Pom1 at the cell tips throughout interphase and then at the division site in anaphase (Figure 4A, second panel from top) as reported previously (Bähler & Pringle, 1998). Time-lapse imaging showed that Pom1 followed the constricting contractile ring and disappeared from the division site after the cells separated. Consequently, after cell division, the concentration of Pom1 was higher at the old cell ends than at the new ends. As the growth of the new ends took off, Pom1 concentrated at the new ends with gradients toward the middles of the cells.

The behavior of Pom1 in the very short *wee1-50* cells grown at 36° C for 4 h and imaged at 22° C was mostly similar to wild-type cells. However, when cells formed a contractile ring, the Pom1 decreased at cell tips as it distributed more homogeneously along the length of the cells. Then it concentrated at the division site and followed the constricting contractile ring as seen in wild-type cells (Figure 4A, upper panel).

The behavior of Pom1 was similar in wild-type, *rga2Δ,* and *rga4*Δ cells grown at 25°C. During interphase, the Pom1-GFP intensity was highest at the tips and low in the middle of the cells. This was exaggerated in the *rga4*Δ cells (Figure 4B, second panel from top). Pom1-GFP accumulated at the division site and followed the cleavage furrow as the cells divided.

During interphase at the nonrestrictive temperature Pom1 concentrated at the cell tips of *cdc25-22* mutant cells as in other strains (Figure 4A, third panel). However, at G_2/M transition the Pom1 concentration decreased at both cell tips, and the fluorescence redistributed homogeneously

385 in the cytoplasm. Similarly, when *cdc25-22* cells were grown at a restrictive temperature of 36°C
386 for 4 h and released at the imaging temperature of 22°C to synchronize them at the G_2/M boundary,
387 Pom1 was initially distributed throughout the cytoplasm (Figure 4A, fourth panel). Then Pom1
388 accumulated at both cell tips peaking during anaphase when the contractile ring formed and
389 matured. Similar to wild-type cells, Pom1 concentrated at the cleavage site and appeared to follow
390 the constricting contractile ring (CS) until it redistributed from the division site to the new ends of
391 daughter cells as they took off and grew (Figure 4A, third and fourth panels).

392 The local intensities of Pom1-mEGFP along the plasma membrane in the broad band did
393 not vary significantly in the five strains with a five-fold range of sizes (Figure 4C) and 100-400
394 nodes (Figure 3H). The local Pom1 concentration did not vary like the Blt1-mCherry intensity
395 along the plasma membrane in the middle focal plane of these cells (Figure 4D). These
396 measurements extend a previous report over a narrower range of cell lengths (Pan et al., 2014).
397 We conclude that during the G_2/M phase transition of the cell cycle the local Pom1 concentration
398 in the broad band does not control the variation in node number with cell size.

399 We used the *nmt81* (no message in thiamine) thiamine-repressible promoter (Maundrell,
400 1993) to control the expression of Pom1 and measured the effects on the cells and their cytokinesis
401 nodes (Figure 5). Pom1 expression was lowest under repressing conditions (EMM5S with
402 thiamine) and 3 times higher than wild-type cells grown in EMM5S without thiamine for 40 h
403 (Figure 5A). The intensity of mEGFP-Pom1 in the broad band along the plasma membrane (Figure
404 5B) and the length of cells undergoing the G_2/M transition (Figure 5C) increased with the average
405 concentration of Pom1 in the cells. The Blt1-mCherry intensity per pixel in the broad band also
406 increased with the Pom1 concentration (Figure 5D), but the unitary node fluorescence measured
407 with Blt1-mCherry did not change (Figure 5E). The width of the broad band of nodes did not
408 change with the total Pom1 (Figure 5F). Therefore, the density of nodes in the broad band increased
409 modestly with the cellular Pom1 concentration as the broad band occupied a smaller fraction of
410 the cell length (Figure 5G). The ratio of the broad band width to the cell length decreased with the
411 total cellular Pom1, indicating that Pom1 controls the width of the broad band (Figure 5H) as
412 expected from previous work (Allard et al., 2019).

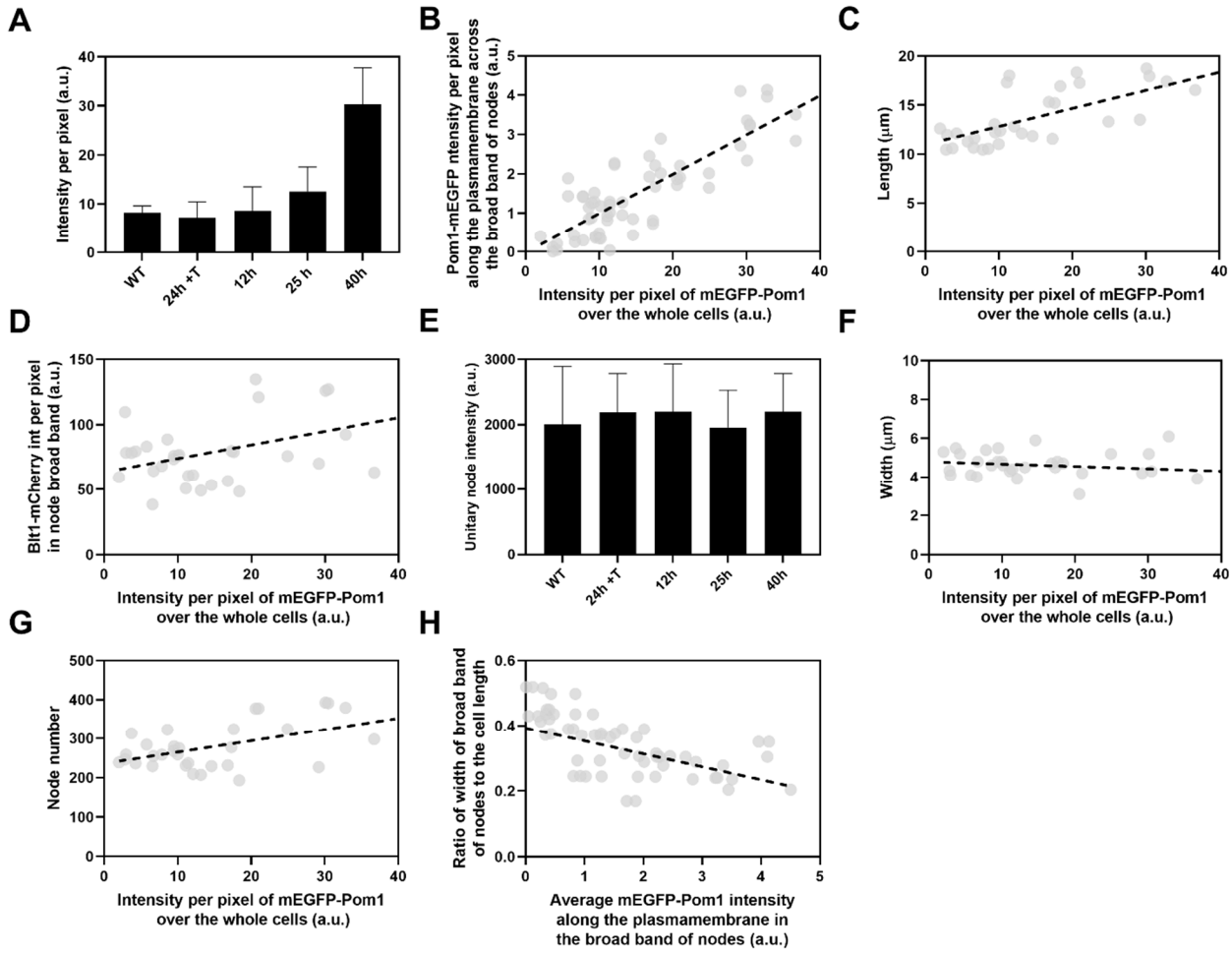

Figure 5. Influence of Pom1 concentration on cell size and numbers of cytokinesis nodes. Expression of mEGFP-Pom1 in cells from the *nmt81* promoter under three conditions: in EMM5S with 5 µg/ml thiamine for 24 h (n = 6 cells) to suppress expression or in EMM5S without thiamine to promote expression for 12 h (n = 6 cells), 25 h (n = 8 cells) or 40 h (n = 8 cells). Grey symbols show individual cells. (A) mEGFP-Pom1 expression under four conditions measured as fluorescence intensity per pixel of mEGFP-Pom1 over the whole cells. (B) Average mEGFP-Pom1 intensity along the plasma membrane in the broad band of nodes in the middle focal plane of the cells as a function of average mEGFP-Pom1 intensity in whole cells. The slope of the linear regression (black dotted line) is significantly nonzero ($P < 0.0001$; $R^2 = 0.7$). (C) Cell length as a function of average mEGFP-Pom1 intensity in whole cells. The slope of the linear regression (black dashed line) is significantly nonzero ($P < 0.0001$; $R^2 = 0.5$). (D) Blt1-mCherry intensity per pixel in node broad band as a function of average mEGFP-Pom1 intensity in whole cells. The slope of the linear regression (black dashed line) is significantly nonzero ($P = 0.01$; $R^2 = 0.2$). (E) Unitary node intensities measured by using Blt1-mCherry in WT cells and cells expressing different levels of Pom1. Error bars are SD, P = 0.001 as determined by Tukey's multiple comparison test. (F) Width of the broad band region as a function of average mEGFP-Pom1 intensity in whole cells. The slope of the linear regression (black dashed line) is significantly zero ($P = 0.3$; $R^2 = 0.04$). (G) Node number as a function of average mEGFP-Pom1 intensity in whole cells. The slope of the linear regression (black dashed line) is significantly nonzero ($P = 0.0017$; $R^2 = 0.3$). (H) Ratio of width of broad band of nodes to the cell length as a function of average mEGFP-Pom1 intensity along the plasma membrane in the broad band of nodes in the middle focal plane of the cells. The slope of the linear regression (black dashed line) is significantly nonzero ($P = 0.0001$; $R^2 = 0.4$).

433 **Does Cdr2 control the number of cytokinesis nodes?**

434 The kinase Cdr2 is the scaffold protein for interphase type 1 nodes, which cluster around the
435 middle of the cell and later merge with type 2 nodes to form cytokinesis nodes. To determine
436 whether the numbers of cytokinesis nodes depend on the concentration of Cdr2, we replaced the
437 Cdr2 promoter in the *S. pombe* genome with the *nmt81* (no message in thiamine) thiamine-
438 repressible promoter (Maundrell, 1993). To quantify Cdr2 expression in these cells the N-terminus
439 of Cdr2 was tagged with mEGFP. This strain also had a C-terminal RFP tag on Sad1 to mark SPBs
440 and a C-terminal mCherry tag on Blt1 to locate and count cytokinesis nodes. Thiamine suppressed
441 the expression of mEGFP-Cdr2 from the *nmt81* promoter while growth without thiamine produced
442 mEGFP-Cdr2 concentrations higher than wild-type cells (Figure 6A).

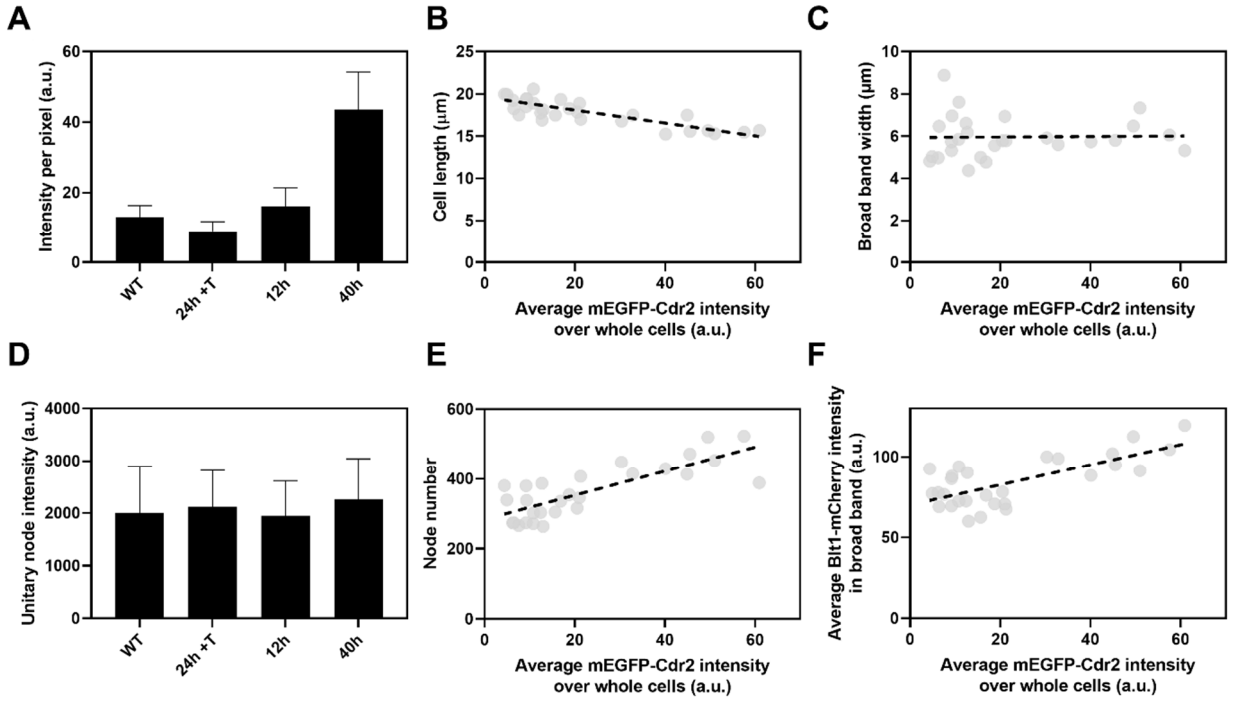

443

444 **Figure 6.** Influence of Cdr2 concentration on cell size and the number of cytokinesis nodes. Expression of mEGFP-
445 Cdr2 in wild-type cells (n = 11 cells) and from the *nmt81* promoter under three conditions: in EMM5S with 5 μg/ml
446 thiamine for 24 h (n = 10 cells) to suppress expression or in EMM5S without thiamine to promote expression for 12
447 h (n = 9 cells) or 40 h (n = 9 cells). Average fluorescence intensities per pixel were measured in sum projection images
448 over whole cells. Grey symbols show individual cells. (A) Average mEGFP-Cdr2 fluorescence intensities per pixel
449 over the whole cells under four conditions. (B) Cell length as a function of average mEGFP-Cdr2 intensity over whole
450 cells. The slope of linear regression (black dashed line) is significantly nonzero ($P < 0.0001$; $R^2 = 0.6$). (C) Width of
451 the broad band of nodes as a function of average mEGFP-Cdr2 intensity over whole cells. The slope of the linear
452 regression (black dashed line) is significantly zero ($P = 0.9$; $R^2 = 0.0004$). (D) Unitary node intensities measured by
453 using Blt1-mCherry in WT cells and cells expressing different levels of Cdr2p. (E) Node number as a function of
454 average mEGFP-Cdr2 intensity over whole cells. The slope of the linear regression (black dashed line) is significantly

455 nonzero (P <0.0001; R^2 = 0.6). (F) Blt1-mCherry intensity per pixel in the broad band area as a function of average
456 mEGFP-Cdr2 intensity over whole cells. The slope of the linear regression (black dashed line) is significantly nonzero
457 (P <0.0001; R^2 = 0.7).

458 The length of the cells as they entered mitosis decreased modestly with the concentration
459 of mEGFP-Cdr2 (Figure 6B), but the width of the broad band of nodes did not change (Figure 6C).
460 The average unitary node intensity measured with Blt1-mCherry in cells grown for 12, 25, or 40
461 h in EMM5S media and 24 h in EMM5S+thiamine did not differ from wild-type cells (Figure 6D).
462 Both the intensity of Blt1-mCherry per pixel in the broad band and the number of cytokinesis
463 nodes increased with the expression of mEGFP-Cdr2 (Figure 6E-F). We conclude that the cellular
464 concentration of Cdr2 has a modest effect on the number and density of cytokinesis nodes and the
465 size of cells entering mitosis but not the width of the broad band of nodes.

466 **Discussion**

467 **Numbers of cytokinesis nodes**

468 Previous work was not clear on the numbers of cytokinesis nodes or the mechanisms that set these
469 numbers. Using Airyscan imaging we measured the number of cytokinesis nodes in *S. pombe* and
470 discovered that the number of cytokinesis nodes is proportional to cell size during early mitosis
471 (Figure 3). Previous studies underestimated the number of cytokinesis nodes due to limitations of
472 imaging techniques and/or methods used to choose nodes (Akamatsu et al., 2014, 2017; Allard et
473 al., 2018; Deng & Moseley, 2013; Laplante et al., 2015; Lenz et al., 2011; Pan et al., 2014;
474 Vavylonis et al., 2008; Willet et al., 2019). Conventional confocal microscopy cannot resolve
475 closely spaced nodes, so confocal images give the impression that cytokinesis nodes vary
476 considerably in size and fluorescence intensity. Several studies considered only the largest nodes
477 when estimating their numbers. On the other hand, super-resolution single-molecule localization
478 microscopy showed that nodes are uniform in size and composition (Laplante et al., 2016).
479 However, the method cannot make a 3D reconstruction of live cells to count the total number of
480 nodes, so the numbers were estimated by extrapolation.

481 Airyscan imaging overcomes these limitations by allowing 3D reconstructions of live cells
482 at a higher resolution than conventional confocal microscopes. We imaged 40 z- slices covering
483 the entire thickness of the cells and used the method of Akamatsu et al. (Akamatsu et al., 2017) to
484 count cytokinesis nodes. The first step was to measure the average fluorescence intensity of a

485 sample of unitary nodes marked with Blt1-mEGFP (Figure 2D). The Airyscan microscope
486 resolved unitary nodes better than the confocal microscope used by Akamatsu et al. (Akamatsu et
487 al., 2017) (Figure 1), so we observed a single peak in the distribution of fluorescence intensities
488 rather than multiple peaks of fluorescence intensity arising from overlapping unitary nodes. These
489 unitary nodes move closer to each other to form binary and multiples of unitary nodes and
490 eventually coalesce into a contractile ring. The second step was to measure the total Blt1-mEGFP
491 fluorescence in the broad band of nodes in the cortex around the equator of the cell, correcting for
492 background cytoplasmic fluorescence. Dividing the total Blt1-mEGFP fluorescence in the broad
493 band by the average fluorescence of a unitary node gave the number of nodes, ~200 unitary nodes
494 in wild-type fission yeast cells.

495 Similar measurements on contractile rings yielded ~150 cytokinesis nodes in wild-type
496 cells (Figure 2E). Therefore, about 75% of total cytokinesis nodes (~200) are incorporated into
497 contractile rings. This may be related to the observation that 10 min before spindle pole bodies
498 divide, 75% of late interphase nodes contained markers of both type 1 and type 2 nodes (Akamatsu
499 et al., 2014) at the time they begin to accumulate Myo2, IQGAP Rng2, F-BAR Cdc15, and formin
500 Cdc12 (J. Q. Wu et al., 2003). During 10-15 min after spindle pole bodies separate, cytokinesis
501 nodes containing these proteins and Blt1 condense into a contractile ring (Vavylonis et al., 2008;
502 J.-Q. Q. Wu et al., 2006). The type 1 node scaffold protein Cdr2 leaves the contractile ring as it
503 forms (Akamatsu et al., 2014). Anillin Mid1 is released from the fully formed contractile rings as
504 unconventional myosin-II Myp2 joins the ring (J. Q. Wu et al., 2003). It is possible that the 25%
505 of cytokinesis nodes with Blt1 but lacking Cdr2 are left behind when the contractile ring forms
506 because they failed to grow actin filaments or were deficient in Myo2, which are required for
507 contractile ring formation.

508 Our approach may be useful to extend studies on how the density of nodes marked with
509 Cdr2 senses surface area, activates cyclin-dependent kinase Cdk1 through inhibitory
510 phosphorylation of *wee1,* and promotes the transition into mitosis (Facchetti, Knapp, Flor-Parra,
511 et al., 2019; Pan et al., 2014; Russell & Nurse, 1987; Simanis & Nurse, 1986). Rather than
512 measuring the total intensity of Cdr2 around the equator (Facchetti, Knapp, Flor-Parra, et al., 2019;
513 Pan et al., 2014; Russell & Nurse, 1987; Simanis & Nurse, 1986) or counting only bright nodes
514 (Pan et al., 2014), we measured the number of unitary nodes marked with Blt1 and found that their

515 density varied with cell sizes except in *cdc25-22* mutant cells (Figure 3K). Using our method to
516 count unitary nodes marked with Cdr2 or Blt1 may provide further insights into the relation of
517 node numbers to the timing of cell division.

518 **Cytokinesis node number in broad bands scales with cell size**

519 Starting from the observation that the number of interphase nodes in wild type cells increases with
520 the two-fold increase in cell size during the cell cycle (Akamatsu et al., 2017; Allard et al., 2018;
521 Deng & Moseley, 2013; Pan et al., 2014), we measured the number of cytokinesis nodes in wild
522 type and mutant cells that varied 5-fold in size as they entered mitosis (Figure 3). To avoid the
523 time-dependent compositional changes in cytokinesis nodes during their ~22-minute life span and
524 to be able to compare the number of cytokinesis nodes as well as the cell size among the wild type
525 and four mutant cells, we restricted our measurements to a specific cell cycle time point. The
526 average fluorescence intensity of the unitary nodes was the same in wild-type and these mutant
527 cells except for the tiny *wee1-50* mutant cells (Figure 3G). The total Blt1-mEGFP fluorescence in
528 broad band of nodes and therefore the total number of nodes increased with cell size measured as
529 volume (Figure 3H) or length (Figure 3I), or surface area (Figure 1—figure supplement 1, A).

530 **Influence of the kinases Pom1 and Cdr2 on the broad band of cytokinesis nodes**
531 We investigated the roles of Pom1, the kinase that restricts type 1 nodes from the poles of cells,
532 and Cdr2, the kinase and scaffold protein for type 1 nodes, in setting the number of cytokinesis
533 nodes. Pom1 forms a gradient from the cell tips to their middles and phosphorylates Cdr2 at
534 multiple sites. Phosphorylation of one site reduces Cdr2 oligomerization and membrane binding
535 at the poles, while phosphorylation of another site inhibits Cdr2 from phosphorylating the Wee1
536 kinase (Bhatia et al., 2014; Deng & Moseley, 2013; Martin & Berthelot-Grosjean, 2009;
537 Moseley et al., 2009; Rincon et al., 2014). However, both *cdr2*Δ and *pom1*Δ cells form nodes
538 and complete cytokinesis, although the cleavage site is off-center in *pom1*Δ cells because they
539 only exclude nodes from one pole by an unknown mechanism (Martin & Berthelot-Grosjean,
540 2009; Moseley et al., 2009).

541 Pan et al. (Pan et al., 2014) found a constant concentration of Pom1 along the equatorial
542 plasma membrane of wild-type cells as they grew two-fold, and we extended the range of sizes to
543 five-fold. Thus, the scaling of interphase or cytokinesis node numbers with cell size is not a
544 consequence of differences in Pom1 in the broad band. Furthermore, Pan et al. (Pan et al., 2014)

545 also reported that total Cdr2 and Cdr2 in interphase nodes increased with cell size during the cell
546 cycle in cells with or without Pom1. This is very strong evidence that Pom1 does not control type
547 1 node formation directly, rather as we explain below, Pom1 controls the cytokinesis node number
548 indirectly via its influence on cell size.

549 Although neither Cdr2 nor Pom1 controls the scaling of interphase node number with cell
550 size, both can influence the number and density of cytokinesis nodes in the broad bands of mitotic
551 cells. Artificially varying the total cellular concentration of Pom1 revealed the following
552 dependencies as cells entered mitosis: the lengths of the cells (Figure 5C), the concentration of
553 Pom1 along the plasma membrane in the broad band (Figure 5B), and the numbers of cytokinesis
554 nodes (Figure 5G) all increased with the cellular concentration of Pom1, while both the
555 fluorescence of unitary nodes (Figure 5E) and the width of the broad band (Figure 5F) were
556 constant. Therefore, high Pom1 increased the density of cytokinesis nodes (Figure 5F) as the broad
557 band occupied a smaller fraction of the cell (Figure 5H). The numbers of cytokinesis nodes in cells
558 expressing high Pom1 concentrations exceeded the numbers in cells of similar lengths and normal
559 Pom1 concentrations (Figure 3I).

560 On the other hand, cells expressing low concentrations of Pom1 were shorter when they
561 divided (Figure 5C) with fewer cytokinesis nodes (Figure 5G) than cells with high Pom1
562 concentrations. The node numbers were higher than in cells of a given length with normal Pom1
563 levels (Figure 3I).

564 Artificially increasing the total cell concentration of Cdr2 (Figure 6) reduced cell length at
565 the time of division (Figure 6B) but did not change the width of the broad band of cytokinesis
566 nodes (Figure 6C), so the broad band occupied a larger fraction of the cell surface. High Pom1
567 concentrations had the opposite effects on cell size (Figure 5C) and broad band width (Figure 5F).
568 On the other hand, the number of cytokinesis nodes increased with the concentration of Cdr2
569 (Figure 6E). The short cells expressing high Cdr2 concentrations had almost double the number of
570 cytokinesis nodes in their slightly wider broad bands than cells of similar lengths with wild-type
571 levels of Cdr2 (Figure 3I). Longer cells expressing low concentrations of Cdr2 had numbers of
572 cytokinesis nodes similar to cells of the same lengths in Figure 3I. The plot of cytokinesis node
573 number vs. Cdr2 concentration extrapolates to more than 200 nodes when the Cdr2 concentration

574 is zero (Figure 6E), as expected for cells longer than wild-type cells at division (Figure 6B).
575 Therefore, Cdr2 can drive cytokinesis node numbers above the basal level of about 200.

576 **Mechanisms**

577 *Cell size dominates in setting the basal number of nodes:* Low SIN activity during interphase is a
578 prerequisite for the assembly of type 1 interphase nodes (Pu et al., 2015), but cell size has a
579 dominant influence in setting the number of nodes in wild-type cells. Accordingly, as cells grow,
580 the number of interphase nodes doubles as they mature into cytokinesis nodes. A limiting amount
581 of an essential node protein might set the number of nodes, but only about half of each of the
582 known node proteins assemble into nodes (Akamatsu et al., 2017). Alternatively, a cell-size-
583 dependent posttranslational modification of one of these proteins may limit the number of nodes.
584 Phosphorylation of the type 1 node scaffold protein Cdr2 by Pom1 is a candidate mechanism, but
585 deletion of Pom1 does not affect the number of nodes (Bhatia et al., 2014; Pan et al., 2014). Nodes
586 turn over continuously, so the rates of node formation and turnover must have a strong influence
587 on their numbers. However, we do not yet know whether one protein at a time or whole nodes turn
588 over or how this process is controlled. All these options are attractive subjects for future research.

589 *Pom1 and Cdr2 modulate a basal number of nodes:* We find that cell size is the primary
590 determinant of the number of cytokinesis nodes (Figure 3) but that the cellular concentrations of
591 the Cdr2 and Pom1 kinases can independently influence cell size and drive the number of
592 cytokinesis nodes above a baseline (Figure 7). The modulating effect of the two kinases is seen in
593 plots of node number vs. the concentrations of either kinase, which intercept the y-axis well above
594 zero (Figures 3H, 5G, and 6E). The presence of a basal number of cytokinesis nodes is expected,
595 since cells without either Cdr2 or Pom1 form cytokinesis nodes (Almonacid et al., 2009; Martin
596 & Berthelot-Grosjean, 2009; Moseley et al., 2009). We propose that interactions of Pom1 and Cdr2
597 modulate the numbers of cytokinesis nodes through their effects on cell size.

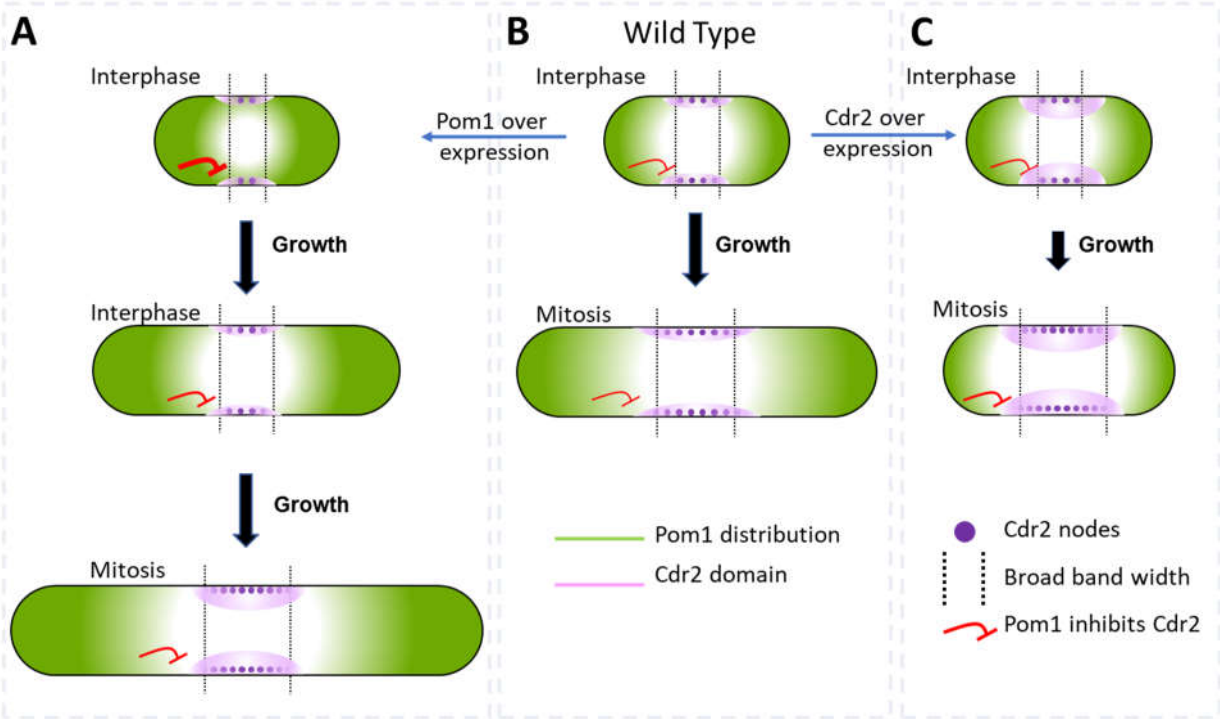

Figure 7. Factors that influence cell size and the broad band of cytokinesis nodes in (B) wild-type cells and cells overexpressing (A) Pom1 or (C) Cdr2. The gradient of Pom1 along the cell plasma membrane is shown in green. The distribution of Cdr2 on the plasma membrane is shown in magenta and called the Cdr2 domain. Purple dots show the density of Cdr2 nodes. Blunt end red lines show the inhibitory action of Pom1 on Cdr2, with the line thickness showing the strength. Lengths of black arrows show the time spent growing. The two dotted lines across the middles of the cells show the borders of the broad band of nodes.

Pom1 regulates interphase node localization by phosphorylating Cdr2, which reduces its oligomerization and membrane binding (Bhatia et al., 2014; Rincon et al., 2014). This direct effect of Pom1 on Cdr2 is one way the gradient of Pom1 from the poles of the cell can restrict nodes to a broad band around the equator (Figure 7B). As cells grow, the overlap of the Pom1 gradient with Cdr2 in the middle of the cell decreases.

In addition, Pom1 regulates cell size at the time of division through a series of three inhibitory phosphorylation reactions: Pom1 phosphorylation inhibits the kinase activity of Cdr2; Cdr2 phosphorylates and inhibits the Wee1 kinase; Wee1 phosphorylates inhibitory sites on Cdk1, the master mitotic kinase that promotes entry into mitosis (Allard et al., 2018; Breeding et al., 1998; Russell & Nurse, 1987). As cells grow, the influence of Pom1 on Cdr2 and Wee1 diminishes, contributing to the activation of Cdk1 and the transition into mitosis (Figure 7B) (Allard et al., 2018, 2019; Martin & Berthelot-Grosjean, 2009; Moseley et al., 2009).

617 Based on these mechanisms, over expression of Cdr2 might increase the number of
618 cytokinesis nodes (Figures 6E and 7C) by mass action. In addition, mass action may drive Cdr2 to
619 inhibit enough Wee1 to promote premature mitosis, resulting in short daughter cells (Figure 6B)
620 with more nodes packed more densely in a broad band of normal width (Figures 6C, 6E, and 7C).
621 Unexpectedly, the number of cytokinesis nodes also increases with the Pom1 concentration
622 (Figure 5G). Based on the Pom1 to Cdk1 pathway, one expects high concentrations of Pom1 to
623 inhibit the assembly of Cdr2 into nodes. However, inhibiting Cdr2 results in high Wee1 activity
624 that inhibits Cdk1, delays the cell cycle, and allows cells to grow longer (Figure 7A). The dominant
625 effect of cell size on driving node formation produces more nodes (Figure 5C).
626 *Pom1 and Cdr2 influence the width of the broad band and density of nodes:* Wild-type
627 cells form type 1 nodes around the daughter nuclei and use a gradient of Pom1 from the poles to
628 confine these nodes to the equator throughout interphase (Figure 7B). As cells elongate during
629 interphase, three parallel events result in two-fold longer cells with twice the number of nodes
630 located in a two-fold wider broad band ready for mitosis. First, the Pom1 concentration on the
631 plasma membrane is low in a zone in the middle of the cell that widens in proportion to a wide
632 range of cell sizes (Figures 3J, 4C and 7B) (Bhatia et al., 2014; Pan et al., 2014). Second, except
633 in *cdc25-22* mutant cells, the density (Figure 3K) and the total number of nodes marked with Blt1
634 (Figure 3H) or Cdr2 (Bhatia et al., 2014; Pan et al., 2014) in this broad band increases with cell
635 size in cells with or without Pom1 (Bhatia et al., 2014; Pan et al., 2014). Third, the broad band
636 widens in proportion to cell size (Figure 3J). Two additional factors contribute to limiting nodes
637 to the equator. One is the uncharacterized activity that excludes nodes from one pole in the absence
638 of Pom1 (Martin & Berthelot-Grosjean, 2009; Moseley et al., 2009). The other is anillin, Mid1,
639 given that nodes spread over the entire plasma membrane in *mid1*Δ cells (Saha & Pollard, 2012).

640 The difference between the *cdc25-22* mutant cells and the other strains in packing their
641 nodes more densely as they grow larger (Figure 3K) may be tied to the experimental conditions.
642 As cells of the other strains move naturally through the cell cycle, their nodes sense the surface
643 area and use the Cdr2-Wee1-Cdk1 pathway to reach the mitotic threshold of node density or
644 number. On the other hand, we hold the *cdc25-22* mutant cells at the G_2/M transition until releasing
645 them into mitosis. As the arrested cells grow at their tips, the extra nodes formed after the threshold
646 time have room to spread out ever further from Pom1 at the cell tips. The large nucleus in the

647 *cdc25-22* mutant cells and the effect of ER-plasma membrane contacts on node distribution (Zhang
648 et al., 2016) need further attention.

649 The concentrations of Pom1 and Cdr2 to Pom1 also influence the width of the broad band
650 and the density of nodes therein (Figure 7). Overexpression of Cdr2 drives both node formation
651 and premature cell division, while the natural level of Pom1-driven inhibition from the poles does
652 not allow space for new nodes at the edges of the broad band, so the surface density of cytokinesis
653 nodes is higher (Figure 7C). Cells over expressing Pom1 also have a higher density of nodes
654 around their equators owing to more nodes (Figure 5G) in broad bands of normal widths (Figure
655 5F). Like short wild-type interphase cells (Figure 7B), overexpression of Pom1 increases its
656 concentration in the middle of cells (Figure 5B) and suppresses the spread of the broad band in
657 spite of delayed mitosis increasing the length of these cells (Figures 5C and 7A).

658 *Influence of cell shape:* The shape of the cell can also influence the number of nodes. For
659 example, the wide but short *rga4Δ* mutant cells lacking the RhoGAP Rga4 are normal in many
660 ways (unitary node intensity, numbers, and densities of nodes for their lengths) but due to their
661 large diameters, they are an outlier with fewer cytokinesis nodes than expected for cells with a
662 given volume. In addition, the gradient of Pom1 from the cell tips is steeper in *rga4Δ* mutant cells
663 than wild-type cells and the Blt1-mCherry+Sad1RFP fluorescence was spread more widely across
664 the middle of *rga4Δ* mutant cells than in wild-type or other strains (Figure 4B, second and third
665 panels from the top).

666 **Incorporation of the proteins of cytokinesis nodes into contractile rings**

667 Most of the proteins comprising cytokinesis nodes during mitosis (Blt1, anillin Mid1, F-BAR
668 Cdc15, IQGAP Rng2, and Myo2) are initially incorporated into contractile rings (Goss et al., 2014;
669 J.-Q. Wu & Pollard, 2005). Thereafter, Myo2 is retained and concentrated along with newly
670 arriving Myp2, while first Mid1 and then subsequently actin are lost in proportion to the declining
671 circumference of the constricting contractile ring (Courtemanche et al., 2016; Malla et al., 2021).
672 This gave the strong impression that the core of the cytokinesis nodes, with the exception of Mid1,
673 remained intact in the contractile ring. However, we report here that the fraction of Blt1 in
674 cytokinesis nodes incorporated into contractile rings varies: nearly 100% in *rga4Δ* mutant cells,
675 75% in wild-type cells, and 25-50% in *cdc25-22*, *wee1-50,* and *rga2Δ* mutant cells. In the case of
676 the longest *cdc25-22* mutant cells, a much larger fraction of the Myo2 from the cytokinesis nodes

677 was incorporated into the rings than Blt1 (Figure 3–figure supplement 2). Arresting and then
678 releasing the cell cycle of the *cdc25-22* mutant cells at the G_2/M transition may contribute to this
679 imbalance, which is greater than in any of the strains allowed to cycle normally. In any case, this
680 new observation indicates that nodes observed in rings by single-molecule localization microscopy
681 are likely to have different compositions than cytokinesis nodes. Documenting and characterizing
682 this maturation of nodes transitioning into contractile rings is worthy of further exploration.

683 **Methods and Materials**

684 **Yeast strains**

685 Table 1 lists the strains used in this work. We used standard methods for *S. pombe* growth and
686 genetics (Moreno et al., 1991). We made most observations on a strain with spindle pole bodies
687 (SPBs) marked by Sad1–RFP, and nodes marked by Blt1-mEGFP (Goss et al., 2014). The
688 sequences encoding the fluorescent proteins were incorporated into the haploid genome, so all
689 copies of these proteins were tagged. The yeast strains *rga2Δ* (FC3158) and *rga4Δ* (FC3157) were
690 a kind gift from the laboratory of Prof. Fred Chang (University of California, San Francisco). All
691 the other strains were obtained from laboratory stocks or by crossing laboratory stock strains.
692 Strains were confirmed by growth on selective media and microscopy. Except for Figures 5 and
693 6, cells were grown in YE5S medium for 24 h at 25°C and then overnight in synthetic EMM5S
694 medium at 25°C before imaging.

695 To control the expression of Cdr2 and Pom1 (Figures 5 and 6), we inserted by homologous
696 recombination the weak *nmt81* promoter along with mEGFP upstream of the open reading frames
697 for Cdr2 or Pom1 in their chromosomal loci. Cells were grown in EMM medium for 25 h at 25°C
698 to induce moderate expression or 40 h at 25°C to over-express mEGFP-Cdr2 or mEGFP-Pom1.
699 Cells were grown in 5 µg/ml thiamine for >24 h at 25°C to repress the expression of these two
700 fusion proteins. The OD_{595} of the cultures was kept below 0.6 over the entire period.

701 **Table 1.** Strains used in this study

Strain	Genotype	Source
WS40	h- blt1-mEGFP:KanMX6 sad1-RFP:KanMX6 ade6-M21X leu1-32 ura4-Δ18	Laboratory Stock
WS46	h- *cdc25-22* blt1-mEGFP:KanMX6 sad1-RFP:KanMX6 ade6-M21X leu1-32 ura4-Δ18	This study

WS47	h- wee1-50 blt1-mEGFP:KanMX6 sad1-RFP:KanMX6 ade6-M21X leu1-32 ura4-Δ18	This study
WS51.1	h- *rga2*Δ blt1-mEGFP:KanMX6 sad1-RFP:KanMX6 ade6-M21X leu1-32 ura4-Δ18	This study
WS52.1	h- *rga4*Δ blt1-mEGFP:KanMX6 sad1-RFP:KanMX6 ade6-M21X leu1-32 ura4-Δ18	This study
WS59	h- pom1-GFP kanMX6 blt1-mCherry natMX6 sad1-mRFP kanMX6 ade6-M21X leu1-32 ura4-Δ18	Laboratory Stock
WS54	h- *rga2Δ* pom1-GFP kanMX6 blt1-mCherry natMX6 sad1-mRFP kanMX6 ade6-M21X leu1-32 ura4-Δ18	This study
WS55	h- *rga4Δ* pom1-GFP kanMX6 blt1-mCherry natMX6 sad1-mRFP kanMX6 ade6-M21X leu1-32 ura4-Δ18	This study
WS56	h- *cdc25-22* pom1-GFP kanMX6 blt1-mCherry natMX6 sad1-mRFP kanMX6 ade6-M21X leu1-32 ura4-Δ18	This study
WS57	h- *wee1-50* pom1-GFP kanMX6 blt1-mCherry natMX6 sad1-mRFP kanMX6 ade6-M21X leu1-32 ura4-Δ18	This study
WS70	h- HygMX6-Pnmt81-mEGFP-Pom1 blt1-mCherry natMX6 sad1-mRFP kanMX6 ade6-M21X leu1-32 ura4-Δ18	This study
WS71	h- KanMX6-Pnmt81-mEGFP-Cdr2 blt1-mCherry natMX6 sad1-mRFP kanMX6 ade6-M21X leu1-32 ura4-Δ19	This study
CL181	h+ KanMX6-Pmyo2-mEGFP-myo2 Sad1-RFP-KanMX6 ade6-M216 his3-D1 leu1- 32 ura4-D18	Laboratory Stock
JW875	h+ cdc25-22 kanMX6-Pmyo2-GFP-myo2 ade6-M210 leu1-32	Laboratory Stock

Airyscan microscopy

Imaging was performed on LSM 880 laser scanning confocal microscope (ZEISS) equipped with 100X Plan Apochromatic 1.46 NA oil objective, an Airyscan super-resolution module, GaAsP detectors, and Zen Black acquisition software (ZEISS). We acquired 40 Z-slices with step size 170 nm covering the entire volume of a cell. Pixel size was 41 nm by 41 nm. Images were collected with pixel dwell time 1.02 μs and image size of 520 x 520 pixels corresponding to 22 × 22 μm. Cells were imaged with 488 nm laser and BP 420-480 excitation /BP 495-620 emission filters for mEGFP; and 561 nm laser and BP 495-550 excitation /LP 570 emission filters for RFP. The pixel dwell time, laser intensity, and detector gain were kept low to avoid saturation and photobleaching during the image acquisition. To increase signal-to-noise ratio and resolution, acquired images were processed by 3D Airyscan filter strength 7.0 with Zen Black software.

713 We identified cytokinesis nodes as spots of Blt1-mEGFP fluorescence around the equator
714 of cells with two SPBs marked by Sad1–RFP, indicating that the cells were in mitosis. We
715 identified and measured the fluorescence intensity of unitary cytokinesis nodes using the following
716 procedure to process the fluorescent images. First, we used ImageJ software to make a maximum
717 intensity projection from 40 Z-slices of Airyscan images containing all of the fluorescence spots
718 in the broad band of a cell (Figure 2A). These spots varied considerably in size and brightness
719 depending on the number of 'unitary nodes' clustered in a diffraction-limited spot (Akamatsu et
720 al., 2017; Laplante et al., 2016). We searched for small spots and marked their X-Y positions. Then
721 we inspected the fluorescence along the Z-axis at these X-Y positions in 40 Z- slices. To qualify
722 as a unitary node, a spot had to satisfy two conditions: 1) the fluorescence of a spot was present
723 within a circle 12 pixels (~0.5 μm) in diameter; and 2) the fluorescence of a spot was present in 7
724 or fewer consecutive Z-slices with a peak in the middle slice and diminishing towards both sides.
725 This middle slice was designated as the Z-axis position of the unitary node. The X-Y-Z positions
726 of each node were stored in the ROI manager of ImageJ software and exported to MATLAB using
727 the add-on @ReadImageJROI developed by (Muir, 2021). We developed a MATLAB code for
728 further analysis (Suppl. Info 1). We sum projected the 7 z-slices containing the unitary node and
729 measured the total fluorescence intensity within circle 12-pixels in diameter the X-Y position of
730 the node (Figure 2B, black dotted circle). From the same sum-projected image we measured the
731 average cytoplasmic fluorescence from 8 circles 12-pixels in diameter from regions of cytoplasm
732 near the cell tips where nodes were absent (Figure 2B, blue dotted circles). We subtracted this
733 average cytoplasmic fluorescence from the node fluorescence to remove the background to obtain
734 fluorescence of a unitary node.

735 To obtain the total fluorescence of a broad band of nodes, we sum projected 40 Z- slices
736 of Airyscan images and measured the fluorescence of an ROI drawn around the broad band of
737 nodes (Figure 2C, Red dashed line area). The mean pixel intensity from polygonal ROIs from each
738 cell tip (Figure 2C Yellow dashed line) was averaged and multiplied by the number of pixels in
739 the broad band ROI to calculate the background fluorescence in the volume of the broad band of
740 nodes. This value was subtracted from the fluorescence in the broad band of nodes to remove the
741 background. To estimate the number of nodes in a cell we divided the total fluorescence of the
742 broad band of nodes after subtracting the background by the average total fluorescence of
743 individual unitary nodes after subtracting the background (Figure 2E).

744 In Figure 3K, we calculated the density of nodes in broad bands by taking into account the
745 cell diameters, which were the same in wild-type, *wee1-50*, and *cdc25-22* mutant cells but larger
746 in *rga4Δ* cells and smaller in *rga2Δ* cells.

747 **Confocal microscopy**

748 To compare the confocal and Airyscan imaging shown in Figure 1 we obtained confocal images
749 using the same Airyscan detector. To make and improve the signal-to-noise ratio comparable to
750 Airyscan microscopy we used the pinhole 0.6 AU, 8X averaging, linear constrained iterative
751 deconvolution, and twice the 488 nm laser intensity implemented in Airyscan imaging. We
752 acquired 20 Z-slices with step size 340 nm covering the entire fluorescence of a cell with pixel
753 size 82 nm by 82 nm. Images were processed for linear constrained iterative deconvolution using
754 the ImageJ plugin 'Deconvolution'.

755 To determine the Pom1 localization in Figure 5, we used an Olympus IX-71 microscope
756 with a 100X, numerical aperture (NA) 1.4 Plan Apo lens (Olympus) and a CSU-X1 (Andor
757 Technology) confocal spinning-disk system equipped with an iXON-EMCCD camera (Andor
758 Technology). We used Coherent OBIS 488 nm LS 20 mW and OBIS 561 nm LS 20 mW lasers
759 for excitation. Images were acquired using Micromanager 1.4 (Edelstein et al., 2014).

760 We acquired 15 Z-slices covering the fluorescence of entire cells every 2-5 min with 0.5
761 μm spacing between slices; 22 μW 561 nm laser power (measured after the objective) and 50 ms
762 exposures; 89 μW 488 laser power and 200 ms exposures. Images were sum projected and
763 corrected for camera noise and uneven illumination. Photobleaching was compensated by
764 choosing a small ROI in both channels that was present in another nondividing cell throughout the
765 acquisition and using the Fiji plugin 'Bleach correction' for Exponential Fitting.

766 We studied cytokinesis nodes in cells during the interval between SPB separation and the
767 formation of the contractile ring. The intensity per pixel of an ROI where no cells were present
768 was subtracted from both channels to remove substrate background intensity. Then a line equal to
769 cell width was drawn along the length of the cell, and a line profile was obtained using the ImageJ
770 -Plot profile plugin, which generated a graph of intensity per pixel across the width of cell vs the
771 cell length. The intensity per pixel of wild-type cells not expressing a fluorescent protein was
772 subtracted from each point to remove auto-fluorescence. .

773 For each strain except in *cdc25-22* mutant strain, 10-12 line profiles were obtained as above
774 and aligned at the centers of the cells before calculating average intensities and SDs. To measure
775 the distributions of the fluorescence from Pom1-GFP or Blt1-mCherry plus Sad1-RFP at different
776 phases of cell cycles of wild-type, *wee1-50,* and *cdc25-22* mutant cells, we plotted the intensities
777 per pixel across the width of cell vs the cell length across the cell cycle (Figure 4B) The
778 temperature-sensitive *cdc25-22* mutant cells were grown at the restrictive temperature of 36°C for
779 4 h and released for imaging at 22°C. These cells had a homogeneous distribution of Pom1 in the
780 cytoplasm but higher on one side of the nucleus than the other. In these cells, the line profiles were
781 flipped so the higher concentration of Pom1 was at one end and aligned on their cell centers before
782 averaging and calculating the SDs of the line profiles (Figure 4B, lower panel). We measured the
783 width of the broad band of cytokinesis nodes as the zone where the Blt1-mEGFP signal was >20%
784 of the peak value.

785 We outlined manually whole cells or the broad band area and used the ImageJ plugin
786 'Measure' to measure the Mean intensity in these areas from the intensity per pixel calculated as
787 the total intensity in all the pixels in a region divided by the number of pixels, which is equivalent
788 to the density (Figure 5 and 6).

789 In Figure 4C the Pom1-mEGFP intensity along the equatorial plasma membrane was
790 measured from the confocal images of the middle focal plane (thickness ~ 0.5 μm) of the cells
791 after subtracting the average background intensity from the area where cells were absent in the
792 same image. A rectangle 3 pixels wide (~ 0.4 μm) and as long as the broad band of nodes was
793 manually drawn over the plasma membrane of cells in the image and used to calculate the Pom1-
794 mEGFP intensity per pixel.

795 In Figure 5B, for the similar analysis as in Figure 4C, the mEGFP-Pom1 intensity was
796 measured from the sum projected image of 3 consecutive middle focal planes (thickness ~ 0.5 μm)
797 of the cells obtained by using Airyscan Imaging. To remove the background, the average pixel
798 intensity from the area where cells were absent in the sum image was subtracted from the image.
799 A rectangle 10 pixel wide (~ 0.4 μm) and as long as the broad band of nodes was manually drawn
800 over the plasma membrane of cells in the image and used to calculate the Pom1-mEGFP intensity
801 per pixel in the broad band as shown in Figure 4C, inset.

802 **Acknowledgments**

Research reported in this publication was supported by the National Institute of General Medical Sciences of the National Institutes of Health under award number R01GM026132. The content is solely the responsibility of the authors and does not necessarily represent the official views of the National Institutes of Health. The authors thank Prof. Chang for the *rga4*Δ and *rga2*Δ cells.

Author contributions

Wasim Sayyad, Conceptualization, Data collection, and analysis; Writing—original draft, Writing—review and editing. Thomas D Pollard, Conceptualization, Writing—review and editing; Resources.

Author ORCIDs

Thomas D Pollard https://orcid.org/0000-0002-1785-2969

Wasim A Sayyad https://orcid.org/0000-0002-6064-2860

816 **References**

817 Akamatsu, M., Berro, J., Pu, K. M., Tebbs, I. R., & Pollard, T. D. (2014). Cytokinetic nodes in
818 fission yeast arise from two distinct types of nodes that merge during interphase. *Journal of*
819 *Cell Biology*, *204*(6), 977–988. https://doi.org/10.1083/jcb.201307174

820 Akamatsu, M., Lin, Y., Bewersdorf, J., & Pollard, T. D. (2017). Analysis of interphase node
821 proteins in fission yeast by quantitative and superresolution fluorescence microscopy.
822 *Molecular Biology of the Cell*, *28*(23), 3203–3214. https://doi.org/10.1091/mbc.e16-07-0522

823 Allard, C. A. H., Opalko, H. E., Liu, K.-W., Medoh, U., & Moseley, J. B. (2018). Cell size–
824 dependent regulation of Wee1 localization by Cdr2 cortical nodes. *Journal of Cell Biology*,
825 *217*(5), 1589–1599. https://doi.org/10.1083/jcb.201709171

826 Allard, C. A. H., Opalko, H. E., & Moseley, J. B. (2019). Stable pom1 clusters form a glucose-
827 modulated concentration gradient that regulates mitotic entry. *ELife*, *8*, 1–27.
828 https://doi.org/10.7554/eLife.46003

829 Almonacid, M., Moseley, J. B., Janvore, J., Mayeux, A., Fraisier, V., Nurse, P., & Paoletti, A.
830 (2009). Spatial Control of Cytokinesis by Cdr2 Kinase and Mid1/Anillin Nuclear Export.
831 *Current Biology*, *19*(11), 961–966. https://doi.org/10.1016/j.cub.2009.04.024

832 Bähler, J., & Pringle, J. R. (1998). Pom1p, a fission yeast protein kinase that provides positional
833 information for both polarized growth and cytokinesis. *Genes and Development*, *12*(9), 1356–
834 1370. https://doi.org/10.1101/gad.12.9.1356

835 Beach, J. R., Shao, L., Remmert, K., Li, D., Betzig, E., & Hammer, J. A. (2014). Nonmuscle
836 myosin II isoforms coassemble in living cells. *Current Biology*, *24*(10), 1160–1166.
837 https://doi.org/10.1016/j.cub.2014.03.071

838 Bhatia, P., Hachet, O., Hersch, M., Rincon, S. A., Berthelot-Grosjean, M., Dalessi, S., Basterra,
839 L., Bergmann, S., Paoletti, A., & Martin, S. G. (2014). Distinct levels in Pom1 gradients limit
840 Cdr2 activity and localization to time and position division. *Cell Cycle*, *13*(4), 538–552.
841 https://doi.org/10.4161/cc.27411

842 Breeding, C. S., Hudson, J., Balasubramanian, M. K., Hemmingsen, S. M., Young, P. G., & Gould,
843 K. L. (1998). The cdr2+ gene encodes a regulator of G2/M progression and cytokinesis in

Schizosaccharomyces pombe. *Molecular Biology of the Cell*, *9*(12), 3399–3415. https://doi.org/10.1091/mbc.9.12.3399

Courtemanche, N., Pollard, T. D., & Chen, Q. (2016). Avoiding artefacts when counting polymerized actin in live cells with LifeAct fused to fluorescent proteins. *Nature Cell Biology*, *18*(6), 676–683. https://doi.org/10.1038/ncb3351

Das, M., Wiley, D. J., Medina, S., Vincent, H. A., Larrea, M., Oriolo, A., & Verde, F. (2007). Regulation of Cell Diameter, For3p Localization, and Cell Symmetry by Fission Yeast Rho-GAP Rga4p. *Molecular Biology of the Cell*, *18*(6), 2090–2101. https://doi.org/10.1091/mbc.e06-09-0883

Deng, L., & Moseley, J. B. (2013). Compartmentalized nodes control mitotic entry signaling in fission yeast. *Molecular Biology of the Cell*, *24*(12), 1872–1881. https://doi.org/10.1091/mbc.E13-02-0104

Edelstein, A. D., Tsuchida, M. A., Amodaj, N., Pinkard, H., Vale, R. D., & Stuurman, N. (2014). Advanced methods of microscope control using μManager software. *Journal of Biological Methods*, *1*(2), e10. https://doi.org/10.14440/jbm.2014.36

Facchetti, G., Knapp, B., Chang, F., & Howard, M. (2019). Reassessment of the Basis of Cell Size Control Based on Analysis of Cell-to-Cell Variability. *Biophysical Journal*, *117*(9), 1728–1738. https://doi.org/10.1016/j.bpj.2019.09.031

Facchetti, G., Knapp, B., Flor-Parra, I., Chang, F., & Howard, M. (2019). Reprogramming Cdr2-Dependent Geometry-Based Cell Size Control in Fission Yeast. *Current Biology*, *29*(2), 350-358.e4. https://doi.org/10.1016/j.cub.2018.12.017

Fantes, P., & Nurse, P. (1977). Control of cell size at division in fission yeast by a growth-modulated size control over nuclear division. *Experimental Cell Research*, *107*(2), 377–386. https://doi.org/10.1016/0014-4827(77)90359-7

Goss, J. W., Kim, S., Bledsoe, H., & Pollard, T. D. (2014). Characterization of the roles of Blt1p in fission yeast cytokinesis. *Molecular Biology of the Cell*, *25*(13), 1946–1957. https://doi.org/10.1091/mbc.E13-06-0300

Gu, Y., & Oliferenko, S. (2019). Cellular geometry scaling ensures robust division site positioning.

Nature Communications, *10*(1). https://doi.org/10.1038/s41467-018-08218-2

Henson, J. H., Ditzler, C. E., Germain, A., Irwin, P. M., Vogt, E. T., Yang, S., Wu, X., & Shuster, C. B. (2017). The ultrastructural organization of actin and myosin II filaments in the contractile ring: New support for an old model of cytokinesis. *Molecular Biology of the Cell*, *28*(5), 613–623. https://doi.org/10.1091/mbc.E16-06-0466

Hickson, G. R. X., & O'Farrell, P. H. (2008). Rho-dependent control of anillin behavior during cytokinesis. *Journal of Cell Biology*, *180*(2), 285–294. https://doi.org/10.1083/jcb.200709005

J.M.MitchisonJ.Creanor. (1971). and J. CREANOR. *Experimental Cell Research*, *67*(2), 368–374. https://doi.org/10.1016/0014-4827(71)90421-6

Jourdain, I., Brzezińska, E. A., & Toda, T. (2013). Fission Yeast Nod1 Is a Component of Cortical Nodes Involved in Cell Size Control and Division Site Placement. *PLoS ONE*, *8*(1). https://doi.org/10.1371/journal.pone.0054142

Kolossov, V. L., Sivaguru, M., Huff, J., Luby, K., Kanakaraju, K., & Gaskins, H. R. (2018). Airyscan super-resolution microscopy of mitochondrial morphology and dynamics in living tumor cells. *Microscopy Research and Technique*, *81*(2), 115–128. https://doi.org/10.1002/jemt.22968

Krakoff, I. H., Brown, N. C., & Reichard, P. (1968). *Inhibition Reductase of Ribonucleoside by Hydroxyurea1 Diphosphate*. 1559–1565.

Laplante, C., Berro, J., Karatekin, E., Hernandez-Leyva, A., Lee, R., & Pollard, T. D. (2015). Three Myosins Contribute Uniquely to the Assembly and Constriction of the Fission Yeast Cytokinetic Contractile Ring. *Current Biology*, *25*(15), 1955–1965. https://doi.org/10.1016/j.cub.2015.06.018

Laplante, C., Huang, F., Tebbs, I. R., Bewersdorf, J., & Pollard, T. D. (2016). Molecular organization of cytokinesis nodes and contractile rings by super-resolution fluorescence microscopy of live fission yeast. *Proceedings of the National Academy of Sciences*, *113*(40), E5876–E5885. https://doi.org/10.1073/pnas.1608252113

Laporte, D., Coffman, V. C., Lee, I. J., & Wu, J. Q. (2011). Assembly and architecture of precursor

900 nodes during fission yeast cytokinesis. *Journal of Cell Biology*, *192*(6), 1005–1021.
901 https://doi.org/10.1083/jcb.201008171

902 Lee, I. J., & Wu, J. Q. (2012). Characterization of Mid1 domains for targeting and scaffolding in
903 fission yeast cytokinesis. *Journal of Cell Science*, *125*(12), 2973–2985.
904 https://doi.org/10.1242/jcs.102574

905 Lenz, M., Gardel, M. L., & Dinner, A. R. (2011). Requirements for contractility in disordered
906 cytoskeletal bundles. *New Journal of Physics*, *14*. https://doi.org/10.1088/1367-
907 2630/14/3/033037

908 Malla, M., Pollard, T. D., & Chen, Q. (2021). Counting actin in contractile rings reveals novel
909 contributions of cofilin and type II myosins to fission yeast cytokinesis. *Molecular Biology*
910 *of the Cell*, *47*(Separate), 84–85. https://doi.org/10.1091/mbc.E21-08-0376

911 Martin, S. G., & Berthelot-Grosjean, M. (2009). Polar gradients of the DYRK-family kinase Pom1
912 couple cell length with the cell cycle. *Nature*, *459*(7248), 852–856.
913 https://doi.org/10.1038/nature08054

914 Maundrell, K. (1993). Thiamine-repressible expression vectors pREP and pRIP for fission yeast.
915 *Gene*, *123*(1), 127–130. https://doi.org/10.1016/0378-1119(93)90551-D

916 Moreno, S., Hayles, J., & Nurse, P. (1989). Regulation of p34cdc2 protein kinase during mitosis.
917 *Cell*, *58*(2), 361–372. https://doi.org/10.1016/0092-8674(89)90850-7

918 Moreno, S., Klar, A., & Nurse, P. (1991). [56] Molecular genetic analysis of fission yeast
919 Schizosaccharomyces pombe. In *Methods in Enzymology* (Vol. 194, Issue C, pp. 795–823).
920 https://doi.org/10.1016/0076-6879(91)94059-L

921 Morrell, J. L., Nichols, C. B., & Gould, K. L. (2004). *The GIN4 family kinase , Cdr2p , acts*
922 *independently of septins in fission yeast*. *1*. https://doi.org/10.1242/jcs.01409

923 Moseley, J. B., Mayeux, A., Paoletti, A., & Nurse, P. (2009). A spatial gradient coordinates cell
924 size and mitotic entry in fission yeast. *Nature*, *459*(7248), 857–860.
925 https://doi.org/10.1038/nature08074

926 Muir, D. (2021). *ReadImageJROI*. GitHub. https://github.com/DylanMuir/ReadImageJROI

927 Neumann, F. R., & Nurse, P. (2007). Nuclear size control in fission yeast. *Journal of Cell Biology*,
928 *179*(4), 593–600. https://doi.org/10.1083/jcb.200708054

929 Nurse, P. (1990). Universal control mechanism regulating cell cycle timing of M-phase. *Nature*,
930 *344*(April), 503–508.
931 https://link.springer.com/content/pdf/10.1038/344503a0.pdf%0Ahttps://www.nature.com/ar
932 ticles/344503a0.pdf

933 Nurse, Paul. (1975). Genetic control of cell size at cell division in yeast. *Nature*, *256*(5518), 547–
934 551. https://doi.org/10.1038/256547a0

935 Pan, K. Z., Saunders, T. E., Flor-Parra, I., Howard, M., & Chang, F. (2014). Cortical regulation of
936 cell size by a sizer cdr2p. *ELife*, *2014*(3), 1–24. https://doi.org/10.7554/eLife.02040

937 Pu, K. M., Akamatsu, M., & Pollard, T. D. (2015). The septation initiation network controls the
938 assembly of nodes containing Cdr2p for cytokinesis in fission yeast. *Journal of Cell Science*,
939 *128*(3), 441–446. https://doi.org/10.1242/jcs.160077

940 Rincon, S. A., Bhatia, P., Bicho, C., Guzman-Vendrell, M., Fraisier, V., Borek, W. E., Alves, F.
941 de L., Dingli, F., Loew, D., Rappsilber, J., Sawin, K. E., Martin, S. G., & Paoletti, A. (2014).
942 Pom1 regulates the assembly of Cdr2-Mid1 cortical nodes for robust spatial control of
943 cytokinesis. *Journal of Cell Biology*, *206*(1), 61–77. https://doi.org/10.1083/jcb.201311097

944 Russell, P., & Nurse, P. (1986). cdc25+ functions as an inducer in the mitotic control of fission
945 yeast. *Cell*, *45*(1), 145–153. https://doi.org/10.1016/0092-8674(86)90546-5

946 Russell, P., & Nurse, P. (1987). Negative regulation of mitosis by wee1+, a gene encoding a protein
947 kinase homolog. *Cell*, *49*(4), 559–567. https://doi.org/10.1016/0092-8674(87)90458-2

948 Saha, S., & Pollard, T. D. (2012). Characterization of structural and functional domains of the
949 anillin-related protein Mid1p that contribute to cytokinesis in fission yeast. *Molecular*
950 *Biology of the Cell*, *23*(20), 3993–4007. https://doi.org/10.1091/mbc.E12-07-0536

951 Simanis, V., & Nurse, P. (1986). The cell cycle control gene cdc2+ of fission yeast encodes a
952 protein kinase potentially regulated by phosphorylation. *Cell*, *45*(2), 261–268.
953 https://doi.org/10.1016/0092-8674(86)90390-9

954 Tatebe, H., Nakano, K., Maximo, R., & Shiozaki, K. (2008). Pom1 DYRK Regulates Localization
955 of the Rga4 GAP to Ensure Bipolar Activation of Cdc42 in Fission Yeast. *Current Biology*,
956 *18*(5), 322–330. https://doi.org/10.1016/j.cub.2008.02.005

957 Tatebe, H., Shimada, K., Uzawa, S., Morigasaki, S., & Shiozaki, K. (2005). Wsh3/Tea4 is a novel
958 cell-end factor essential for bipolar distribution of tea1 and protects cell polarity under
959 environmental stress in S. pombe. *Current Biology*, *15*(11), 1006–1015.
960 https://doi.org/10.1016/j.cub.2005.04.061

961 Vavylonis, D., Wu, J.-Q., Hao, S., O'Shaughnessy, B., & Pollard, T. D. (2008). Assembly
962 Mechanism of the Contractile Ring for Cytokinesis by Fission Yeast. *Science*, *319*(5859),
963 97–100. https://doi.org/10.1126/science.1151086

964 Villar-Tajadura, M. A., Coll, P. M., Madrid, M., Cansado, J., Santos, B., & Pérez, P. (2008). Rga2
965 is a Rho2 GAP that regulates morphogenesis and cell integrity in S. pombe. *Molecular*
966 *Microbiology*, *70*(4), 867–881. https://doi.org/10.1111/j.1365-2958.2008.06447.x

967 Werner, M., Munro, E., & Glotzer, M. (2007). Astral Signals Spatially Bias Cortical Myosin
968 Recruitment to Break Symmetry and Promote Cytokinesis. *Current Biology*, *17*(15), 1286–
969 1297. https://doi.org/10.1016/j.cub.2007.06.070

970 Willet, A. H., DeWitt, A. K., Beckley, J. R., Clifford, D. M., & Gould, K. L. (2019). NDR Kinase
971 Sid2 Drives Anillin-like Mid1 from the Membrane to Promote Cytokinesis and Medial
972 Division Site Placement. *Current Biology*, *29*(6), 1055-1063.e2.
973 https://doi.org/10.1016/j.cub.2019.01.075

974 Wu, J.-Q., & Pollard, T. D. (2005). Counting cytokinesis proteins globally and locally in fission
975 yeast. *Science (New York, N.Y.)*, *310*(5746), 310–314.
976 https://doi.org/10.1126/science.1113230

977 Wu, J.-Q. Q., Sirotkin, V., Kovar, D. R., Lord, M., Beltzner, C. C., Kuhn, J. R., & Pollard, T. D.
978 (2006). Assembly of the cytokinetic contractile ring from a broad band of nodes in fission
979 yeast. *Journal of Cell Biology*, *174*(3), 391–402. https://doi.org/10.1083/jcb.200602032

980 Wu, J. Q., Kuhn, J. R., Kovar, D. R., & Pollard, T. D. (2003). Spatial and temporal pathway for
981 assembly and constriction of the contractile ring in fission yeast cytokinesis. *Developmental*

982 *Cell*, *5*(5), 723–734. https://doi.org/10.1016/S1534-5807(03)00324-1

983 Ye, Y., Lee, I.-J., Runge, K. W., & Wu, J.-Q. (2012). Roles of putative Rho-GEF Gef2 in division-
984 site positioning and contractile-ring function in fission yeast cytokinesis. *Molecular Biology*
985 *of the Cell*, *23*(7), 1181–1195. https://doi.org/10.1091/mbc.e11-09-0800

986 Zhang, D., Bidone, T. C., & Vavylonis, D. (2016). ER-PM Contacts Define Actomyosin Kinetics
987 for Proper Contractile Ring Assembly. *Current Biology*, *26*(5), 647–653.
988 https://doi.org/10.1016/j.cub.2015.12.070

989

990 Figure 3–figure supplement 1

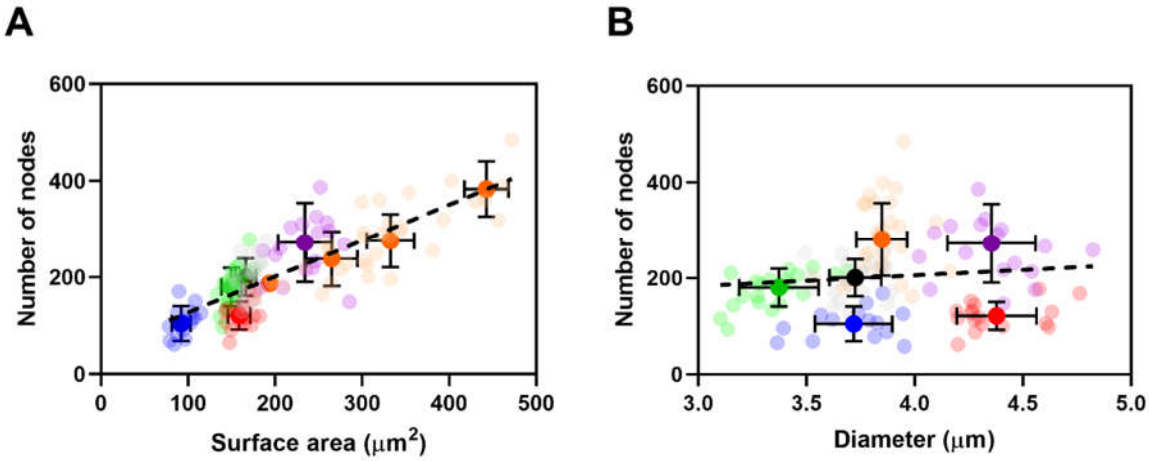

991

992 **The number of cytokinesis nodes scales with the surface area of the cell.**

993 (A-B) Relationships between Node number and cell size parameters (surface area and diameter) in five strains: (●)
994 *wee1-50* (n = 16 cells); (●) *rga2Δ* at (n = 23 cells); (●) wild type at (n = 24 cells); (●) r*ga4Δ* at (n = 17 cells); and (
995 ●) *rga4Δ*+HU (n = 17 cells) at 25°C. (A) Node number vs. surface area. All measurements for each strain are collected
996 in one bin except for (●) *cdc25-22* cells, which are divided into four surface area bins: 200-300 μm^3, n = 11 cells;
997 300-400 μm^3, n = 13 cells; >400 μm^3, n = 6 cells. The transparent symbols are measurements of individual cells. The
998 solid symbols are the mean numbers of node parameters. Except for the *cdc25-22* cells, the vertical error bars show
999 the SD of the mean numbers and horizontal error bars the SD of the lengths. For the *cdc25-22* (volume > 400 μm^3)
1000 cells the error bar is the range. The dashed black lines are linear regressions using all the data points. The slope of the
1001 linear regression (black dashed line) is significantly nonzero ($P < 0.0001$; $R^2 = 0.7$). (B) Node number vs. cell diameter.
1002 All measurements for each strain are collected in one bin. The slope of the linear regression (black dashed line) is
1003 significantly zero ($P = 0.24$; $R^2 = 0.01$).

1004 Figure 3–figure supplement 2

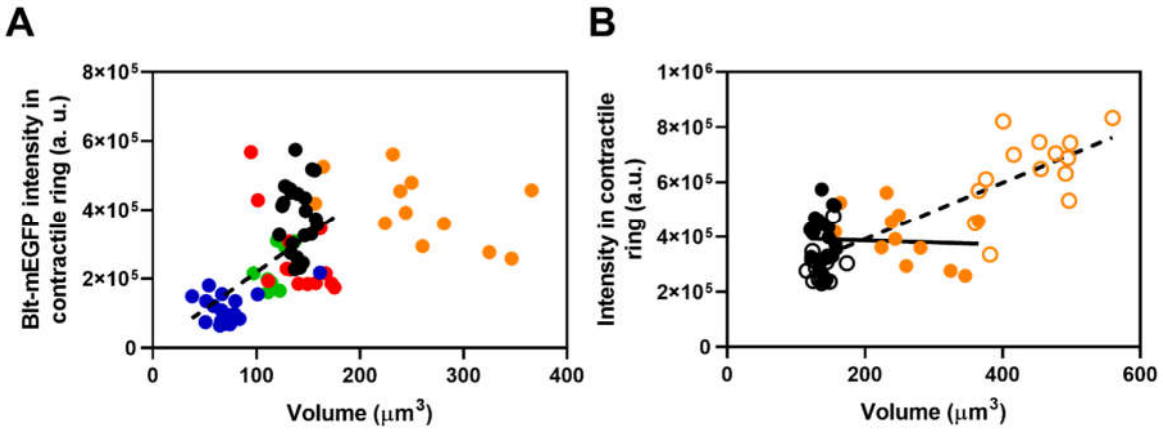

1005

1006 **Fluorescence intensity in the contractile rings of five yeast strains as a function of cell volume**. (A) Blt1-mEGFP
1007 intensity in contractile ring vs. cell volume: (●) *wee1-50*; (●) *rga2Δ*; (●) wild type; (●) r*ga4Δ*; and (●) *cdc25-22*
1008 mutant cells. The slope of the linear regression to all but the orange data points (black dashed line) is significantly
1009 nonzero ($P < 0.001$; $R^2 = 0.3$). (B) Fluorescence intensity of Blt1-mEGFP in contractile rings of (●) wild type and (●
1010) *cdc25-22* mutant cells from panel (A) and fluorescence intensity of mEGFP-Myo2 in contractile rings of (○) wild
1011 type and (○) *cdc25-22* mutant cells vs. cell volumes. The slope of the linear regression to all empty circle data points
1012 (black dashed line) is significantly nonzero ($P < 0.001$; $R^2 = 0.8$). The slope of the linear regression to all filled circle
1013 data points (solid black line) is significantly zero ($P = 0.8$; $R^2 = 0.003$).